

Supporting information for

Poly(ionic liquid)-based aerogels for continuous-flow CO₂ upcycling

Raquel V. Barrulas^a, Christopher Tinajero^b, Diogo P. N. Ferreira^a, Carlos Illanes-Bordomás^d, Victor Sans^b, Manuela Ribeiro Carrott^c, Carlos A. García-González^d, Marcileia Zanatta^{b}, Marta C. Corvo^{a*}*

^a i3N|Cenimat, Department of Materials Science (DCM), NOVA School of Science and Technology, NOVA University Lisbon, 2829-516 Caparica, Portugal

^b Institute of Advanced Materials (INAM), Universitat Jaume I, Avda Sos Baynat s/n, 12071 Castellón, Spain

^c LAQV-REQUIMTE, Institute for Research and Advanced Studies, Department of Chemistry and Biochemistry, School of Sciences and Technology, University of Évora, 7000-671 Évora, Portugal

^d AerogelsLab, Department of Pharmacology, Pharmacy and Pharmaceutical Technology, I+D Farma Group (GI-1645), Faculty of Pharmacy, iMATUS and Health Research Institute of Santiago de Compostela (IDIS), Universidade de Santiago de Compostela, E-15782 Santiago de Compostela, Spain

*Corresponding authors. E-mail address: zanatta@uji.es (Marcileia Zanatta). Tel.: +351 21 294 8562; fax: +351 21 294 8558. E-mail address: marta.corvo@fet.unl.pt (Marta C. Corvo).

Index

1	Synthesis of IL monomers.....	4
2	Synthesis of poly(ionic liquids) (PILs)	5
3	General characterisation protocols	6
3.1	CO ₂ capture experiments using thermogravimetric analysis.....	7
4	General characterisation of materials	7
4.1	BJH-pore size distribution and nitrogen adsorption-desorption isotherm.....	10
4.2	Elemental Analysis.....	11
4.3	FTIR-ATR of PILs and <i>AEROPILs</i>	11
4.4	TGA curves	12
4.5	Solid-state NMR analysis	14
5	Supercritical drying apparatus from Paralab	15
6	Morphological and textural properties of the chitosan aerogels	15
7	CO ₂ capture	17
8	Catalysis	19
8.1	GC-MS Analysis	19
8.2	NMR spectra	21
8.3	Catalyst Regeneration	22
8.4	Continuous flow CO ₂ cycloaddition.....	25
8.5	Catalytic cycle.....	27
9	References	27

1 Synthesis of IL monomers

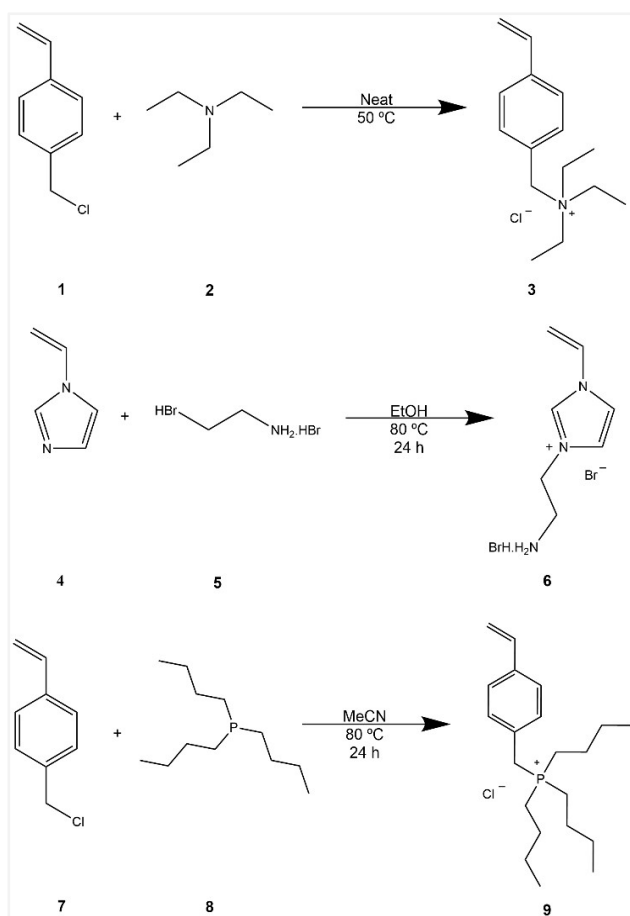


Figure S.1. Synthesis of *p*-vinylbenzyltriethylammonium chloride (**3**), 1-aminoethyl-3-vinylimidazolium bromide hydrobromide (**6**) and *p*-vinylbenzyltributylphosphonium chloride (**9**).

Compound (**3**) *p*-vinylbenzyltriethylammonium chloride ([VBA]Cl) was synthesised according to procedures described in the literature [1,2]. **3** was obtained from the reaction of 4-vinylbenzyl chloride (2.0 g, 13.1 mmol) and triethylamine (1.33 g, 13.1 mmol), at 50 °C under N₂ atmosphere and stirring for 19 h. The precipitated solid was collected, washed with diethyl ether and vacuum-dried. The final compound was obtained with a yield of 91%.

Compound (**6**) 1-aminoethyl-3-vinylimidazolium bromide hydrobromide ([AEIM]Br.HBr) was synthesised according to procedures described in the literature [3,4]. **6** was obtained from the reaction of 1-vinylimidazole (1.57 g, 17 mmol), dissolved in 10 mL of ethanol, and 2-bromoethylamine hydrobromide (3.42 g, 17 mmol), which was only added after refluxing under N₂ atmosphere. The mixture was refluxed for 24 h, and upon cooling, the resulting white precipitate was separated by centrifugation, followed by extensive washing with ethanol. The final compound was obtained with a yield of 100% after drying under vacuum at 120 °C for 12 h.

Compound (**9**) *p*-vinylbenzyltributylphosphonium chloride ([VBP]Cl) was synthesised according to a procedure described in the literature [5]. **9** was obtained from the reaction of 4-vinylbenzyl chloride (1.36 g, 8.94 mmol) and tributylphosphine (1.07 g, 5.27 mmol) dissolved in 10 mL of acetonitrile at 80 °C under N₂ atmosphere and stirring for 24 h. The solvent was removed under vacuum. The precipitate was collected, washed with diethyl ether and vacuum-dried. The final compound was obtained with a yield of 76%.

^1H and ^{13}C NMR and FTIR-ATR confirmed the final structures of **3**, **6** and **9**.

2 Synthesis of poly(ionic liquids) (PILs)

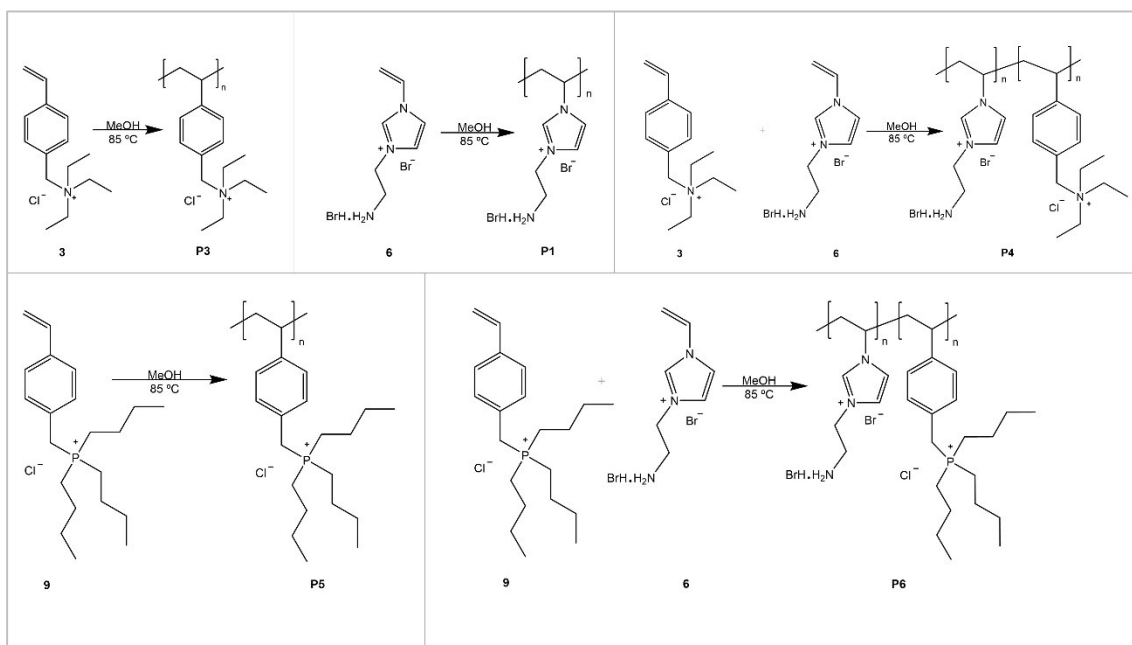


Figure S.2. Synthesis of PILs **P3**, **P1**, **P4**, **P5** and **P6**, respectively.

PILs from monomers **3**, **6** and **9**, namely, poly(*p*-vinylbenzyltriethylammonium) chloride (**P3**), poly(1-aminoethyl-3-vinylimidazolium) bromide hydrobromide (**P1**), copolymer_{50/50} poly(*p*-vinylbenzyltriethylammonium chloride-co-aminoethylimidazolium bromide hydrobromide) (**P4**), poly(*p*-vinylbenzyltributylphosphonium chloride) (**P5**) and copolymer_{50/50} poly(*p*-vinylbenzyltributylphosphonium chloride-co-aminoethylimidazolium bromide hydrobromide) (**P6**) were synthesised according to a procedure described in the literature [6].

P3 was obtained from the reaction of **3** (1.02 g, 4 mmol), AIBN (22 mg, 0.13 mmol) in methanol (2.4 mL). The solution was then heated under N_2 atmosphere for 25 h at 85 °C. The polymerisation was stopped by rapid cooling of the reaction mixture, and the polymer was precipitated with excess cold ethyl acetate, yielding 93%, with a purity of 93% (residual monomer determined by ^1H NMR).

P1 was obtained from the reaction of **6** (1.00 g, 3.37 mmol), AIBN (30 mg, 0.18 mmol) in methanol (12 mL). The solution was then heated under N_2 atmosphere for 4 h at 85 °C. The polymerisation was stopped by rapid cooling of the reaction mixture, and the polymer was dried under vacuum, yielding 100%, with purity 81% (residual monomer determined by ^1H NMR).

P4 was obtained from the reaction of **3** (0.63 g, 2.49 mmol) with **6** (0.63 g, 2.12 mmol), AIBN (30 mg, 0.18 mmol) in methanol (12 mL). The solution was then heated under N_2 atmosphere for 18 h at 85 °C. The polymerisation was stopped by rapid cooling of the reaction mixture, and the polymer was dried under vacuum, yielding 100%.

P5 was obtained from the reaction of **9** (1.27 g, 3.59 mmol), AIBN (55 mg, 0.33 mmol) in methanol (20 mL). The solution was then heated under N_2 atmosphere for 48 h at 95 °C. The polymerisation was stopped by rapid cooling of the reaction mixture, and the polymer was precipitated with excess cold ethyl acetate and dried under vacuum, with a yield of 95%, with purity 95% (residual monomer determined by ^1H NMR).

P6 was obtained from the reaction of **9** (1.12 g, 3.16 mmol) with **6** (1.12 g, 3.77 mmol), AIBN (60 mg, 0.37 mmol) in methanol (20 mL). The solution was then heated under N_2 atmosphere for

48 h at 95 °C. The polymerisation was stopped by rapid cooling of the reaction mixture, and the polymer was dried under vacuum, yielding 98%.

3 General characterisation protocols

Photographs of chitosan beads' morphology in hydrogel, alcogel, and aerogel states were acquired using a digital camera. Subsequent analysis was performed employing ImageJ v1.53e software, developed by the U.S. National Institutes of Health in Bethesda, MD, USA. This analysis aimed to ascertain the diameter and volume of the beads, facilitating the computation of volume reduction throughout each processing phase. Data were derived from the examination of a minimum of approximately 14 beads. The aerogel beads' envelope density (ρ_{env}) was computed as the ratio between the average mass of particles determined through a precision balance (model: 80A-200 M, Precisa, Dietikon, Switzerland) and the dimensions extracted through image analysis.

The determination of skeletal density (ρ_{skel}) involved utilising helium pycnometry (MPY-2, Quantachrome, Delray Beach, FL, USA) conducted at 25 °C and 1.03 bar, with measurements performed on five independent samples. The overall porosity (ε) of the dried gels was quantified as a percentage and computed following the principles outlined in Equation 1:

$$(1) \quad \varepsilon = [1 - (\rho_{\text{env}}/\rho_{\text{skel}})] \times 100$$

The topographical characteristics of the aerogel beads' surface were analysed through SEM microscopy at an accelerating voltage of 3 kV, utilising a secondary electron detector (EVO LS15, Zeiss, Oberkochen, Germany). To enhance contrast, a fine coating of iridium with a thickness of 10 nm was deposited onto the aerogels by sputter coating (Q150 T S/E/ES, Quorum Technologies, Lewes, UK).

SEM images of the reused aerogel beads were acquired using a Hitachi Regulus 8220 Scanning Electron Microscope (Mito, Japan) equipped with energy-dispersive X-ray spectroscopy (EDS) equipment from Oxford Instruments. The reused aerogel beads were previously sputtered coated (Q150 T S/E/ES, Quorum Technologies, Lewes, UK) with a thin layer (15 nm) of iridium to improve the contrast.

The textural properties of the aerogel beads were characterised by nitrogen adsorption-desorption analysis (ASAP 2000, Micromeritics, Norcross, GA, USA). The Brunauer–Emmet–Teller (BET) and the Barrett–Joyner–Halenda (BJH) methods were applied to calculate the specific surface area (a_{BET}) and the pore size distribution, respectively [7]. The overall specific pore volume ($V_{\text{p,BJH}}$) and the mean pore diameter ($D_{\text{p,BJH}}$) were also obtained from the desorption branch by the BJH method. The specific mesopore volume (V_{mes}) was obtained from the cumulative BJH-pore volume profiles of the aerogels in the mesopore range (2–50 nm). The specific volume occupied by the macropores (V_{MP}) in the aerogels was calculated as the difference between the total specific pore volumes of the aerogels (i.e., the inverse of the envelope density) and the specific pore volume occupied by mesopores (V_{mes}).

ATR-FTIR spectra were acquired using a Gladi-ATR accessory equipped with a diamond crystal (Pike, Madison, WI, USA) with 32 scans per spectrum with a spectral resolution of 2 cm^{-1} , covering the 4000 to 400 cm^{-1} range. The samples were directly positioned within the IR laser beam within the sample holder. The acquired spectra were subsequently processed utilising SpectraGryph 1.2.15 software. The aerogels' carbon, hydrogen, and nitrogen contents were obtained with a Thermo Finnigan-CE Instruments Flash EA 1112 elemental analyser.

Raman spectroscopic data were collected using a *Raman Confocal Microscope*, model *apyron* (*WITec*). The system incorporated three optical fibres linked to distinct laser sources for sample

excitation at 532 nm. These laser outputs were filtered using long-pass filters. Two finely tuned spectrometers were employed: the first for the visible spectral range, featuring an EMCCD ultra-high efficiency detector, and the second optimised for the near-infrared (NIR) region, equipped with a high-efficiency CCD detector. This second spectrometer was furnished with diverse Zeiss optical lenses, including x10, x20 LD (long-distance), x50 LD, and x100 LD, to cater to varying focal lengths.

Solid state ^{13}C MAS NMR spectra were acquired utilising an 11.7 T (500 MHz) AVANCE III Bruker spectrometer, operating at 125 MHz (^{13}C), and equipped with a BBO probe head. The experimental setup involved spinning the samples at the magic angle at a frequency of 5 kHz, using 4 mm diameter rotors at room temperature. The ^{13}C MAS NMR experiments were acquired with proton cross-polarisation and total suppression of sidebands or sideband elimination by temporary interruption of the chemical shift (CP-TOSS or SELTICS) with a contact time of 2.0 ms and a recycle delay of 5.0 s. Data processing was carried out using Bruker Topspin 3.6.2 software.

3.1 CO_2 capture experiments using thermogravimetric analysis

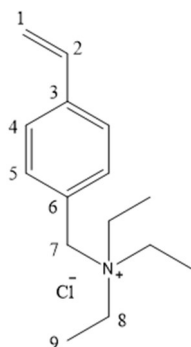
TGA and CO_2 capture experiments were conducted utilising a PerkinElmer STA6000 thermogravimetric analyser controlled through PYRIS v.9.1 software. The TGA profiles were acquired employing a heating rate of $10\text{ }^\circ\text{C min}^{-1}$ under a He flow of 20 mL min^{-1} . Before commencing the CO_2 capture assessments, the samples underwent preheating at $120\text{ }^\circ\text{C}$ and were subjected to a He flow of 100 mL min^{-1} . Following cooling to $25\text{ }^\circ\text{C}$ within He atmosphere, the CO_2 capture protocol was executed as follows: the sample was under a 100 mL min^{-1} flow of He for 10 min; then, the gas was switched to pure CO_2 (100 mL min^{-1}) and left for 10 min; subsequently, the gas was switched back to He (100 mL min^{-1}) and left for 40 min. After these steps, the sample was reheated to $120\text{ }^\circ\text{C}$ under a He atmosphere, cooled again to $25\text{ }^\circ\text{C}$, and a second adsorption-desorption cycle was performed. Control runs that did not involve samples were conducted to account for variations in buoyancy between He and CO_2 conditions.

4 General characterisation of materials

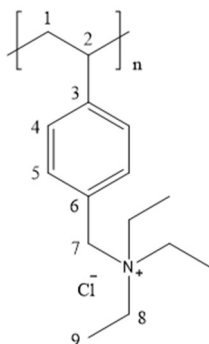
NMR data were acquired at 298.2 K in a Bruker Avance III 400 spectrometer functioning at 400.15 MHz Larmor frequency for hydrogen and 100.61 MHz for carbon either in a Bruker High-Resolution BB-H&F-D-05DIFF probe or BBF-H-D-05ZPlus. This spectrometer is equipped with a temperature control unit and a pulse field gradient unit capable of producing magnetic pulsed field gradients in the z-direction of 50.0 G/cm . Data was processed using Bruker Topspin 3.6.2 software. Spectra description states the deuterated solvent used and, for each signal, chemical shift value, multiplicity, and integration. The following abbreviations indicated signal multiplicity: s, singlet; d, doublet; t, triplet; q, quartet; m, multiplet. $^1\text{H-NMR}$ experiments were acquired with 64 K time domain points over a spectral window of 8012.820 Hz (20.0244 ppm) centred at 2471.09 Hz (6.175 ppm) and with 32 scans per FID; the relaxation delay was set in 1.0 s. $^{13}\text{C-NMR}$ experiments were acquired with 64 K time domain points over a spectral window of 24038.46 Hz (238.88 ppm) centred at 10060.84 (99.991 ppm) with variable scans per FID (1024 to 7168), the relaxation delay was variable, and from 1.5 s until 5.0 s.

ATR-FTIR spectra were recorded on a PerkinElmer Spectrum Two (Waltham, MA, USA) with 8 scans in the $4000\text{ to }400\text{ cm}^{-1}$ range. The samples were placed in the sample holder directly in the IR laser beam. Spectra were processed using SpectraGryph 1.2.15 software. According to the most intense and characteristic vibrations, data are shown as follows: maximum frequency

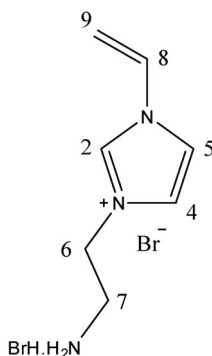
absorption, ν_{\max} , in cm^{-1} (functional group), intensity and shape (s, strong; m, medium; w, weak; ar, aromatic; sy, symmetric).



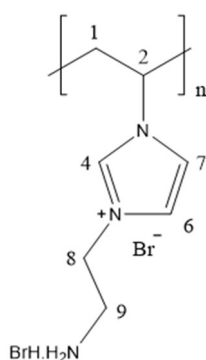
[VBA]Cl (**3**): $^1\text{H-NMR}$ (400 MHz, DMSO- d_6) δ ppm 7.56 (m, 4H, $\text{H}_{4,4'}+\text{H}_{5,5'}$), 6.80 (dd, $J=17.6$ Hz and $J=11.0$ Hz, 1H, H_2), 5.96 (d, $J=17.7$ Hz, 1H, H_1), 5.38 (d, $J=11.0$ Hz, 1H, H_1'), 4.53 (s, 2H, H_7), 3.19 (q, $J=7.2$ Hz, 6H, $\text{H}_{8,8',8''}$), 1.31 (t, $J=7.1$ Hz, 9H, $\text{H}_{9,9',9''}$). $^{13}\text{C-NMR}$ (101 MHz, DMSO- d_6) δ ppm 139.2 (C_3), 136.2 (C_2), 133.4 ($\text{C}_{5,5'}$), 127.8 (C_6), 127.0 ($\text{C}_{4,4'}$), 116.7 (C_1), 59.7 (C_7), 52.5 ($\text{C}_{8,8',8''}$), 8.1 ($\text{C}_{9,9',9''}$). **ATR-FTIR** ν_{\max} cm^{-1} 3401 (OH stretching, H_2O), 3075 (w), 2980 (s, -CH stretching), 1515 (m), 1478 (m, N-($\text{CH}_2\text{-CH}_3$) $_3$), 1463 (s), 1411 (m, -C-N stretching), 1399 (s, C=C), 1295 (w, N- CH_2 -), 1152 (m, ring -CH in-plane), 1010 (s), 945 (m), 862 (s, ar -CH), 808 (s, ar -CH).



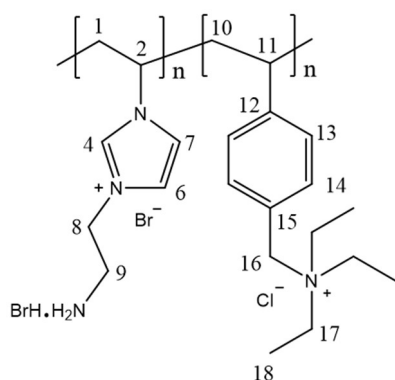
P[VBA]Cl (**P3**): $^1\text{H-NMR}$ (400 MHz, DMSO- d_6) δ ppm 7.58-7.26 (br, $\text{H}_{4,4'}$), 6.89-6.32 (br, $\text{H}_{5,5'}$), 5.05-4.33 (br, H_7), 3.34-3.13 (br, $\text{H}_2+\text{H}_{8,8',8''}$), 1.83-0.90 (br, $\text{H}_1+\text{H}_{9,9',9''}$). $^{13}\text{C-NMR}$ (101 MHz, DMSO- d_6) δ ppm 136.2 (ar, C_5), 132.9 (br, C_4), 128.1 (br, $\text{C}_{5'}$), 126.5 (ar, C_4'), 60.2 (C_7), 58.2 (C_2), 52.4 ($\text{C}_{8,8',8''}$), 49.0 (C_1), 8.1 ($\text{C}_{9,9',9''}$). **ATR-FTIR** ν_{\max} cm^{-1} 3771 (br, m, OH stretching, H_2O), 2983 (m, -CH stretching), 2926 (m, -CH stretching), 1732 (m, ar), 1613 (w, ar), 1514 (w), 1484 (s), 1455 (s), 1397 (s), 1373 (s), 1243 (s), 1156 (m), 1097 (m), 1037 (s), 1011 (s), 847 (m, ar -CH), 824 (m, C-H bend benzene ring), 783 (s, C-H bend benzene ring), 588 (br, s).



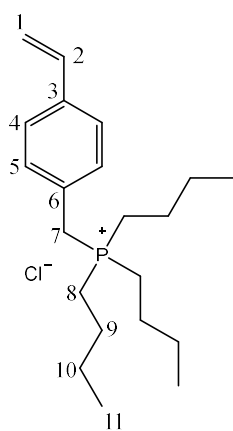
[AEIM]Br.HBr (**6**): $^1\text{H-NMR}$ (400 MHz, D_2O) δ ppm 9.17 (s, 1H, H_2), 7.82 (s, 1H, H_5), 7.66 (s, 1H, H_4), 7.12 (dd, $J=15.6$ Hz and $J=8.6$ Hz, 1H, H_8), 5.80 (dd, $J=15.7$ Hz and $J=2.9$ Hz, 1H, H_9), 5.43 (dd, $J=8.6$ Hz and $J=2.8$ Hz, 1H, H_9'), 4.60 (t, $J=6.3$ Hz, 2H, H_6), 3.56 (t, $J=6.3$ Hz, 2H, H_7). $^{13}\text{C-NMR}$ (101 MHz, D_2O) δ ppm 135.4 (C_2), 128.1 (C_8), 122.9 (C_4), 120.4 (C_5), 110.3 (C_9), 46.7 (C_6), 38.7 (C_7). **ATR-FTIR** ν_{\max} cm^{-1} 3389 (m, -NH stretching), 2944 (s, -CH stretching), 2867 (s, sy, -CH), 1554 (s, - CH_{aliph}), 1441 (m, -C-N stretching), 1368 (w, C=C), 1310 (w, N- CH_2 -), 1167 (s, ring -CH in-plane), 1018 (m), 955 (m), 826 (m, ar -CH), 755 (s, ar -CH).



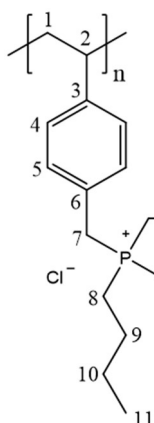
P[AEIM]Br.HBr (**P1**): $^1\text{H-NMR}$ (400 MHz, DMSO- d_6) δ ppm 10.17-9.38 (br, H₄), 8.83-7.63 (br, H₆+H₇), 5.02-4.30 (br, H₂+H₈), 3.83-3.09 (br, H₁+H₉). **ATR-FTIR** ν_{max} cm^{-1} 3389 (br, m, -NH stretching), 2944 (s, -CH stretching), 2867 (s, -CH stretching), 1991 (w, ar), 1651 (m, ar), 1554 (s, -C=N stretching), 1441 (s), 1368 (m), 1310 (m), 1167 (s, -CH in-plane), 1018 (m), 955 (m, ar -CH), 826 (m, C-H bend imidazolium ring), 644 (s, -CH out-of-plane).



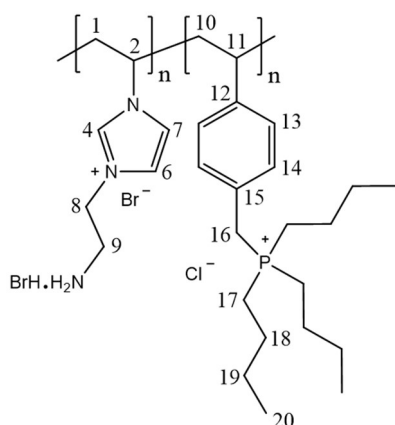
Ammonium co-PIL_{50/50} (**P4**): $^1\text{H-NMR}$ (400 MHz, DMSO- d_6) δ ppm 9.09-8.52 (br, H₄), 8.33-8.23 (br, H₆+H₇+H_{13,13'}), 7.62-6.35 (br, H_{14,14'}), 4.98-4.20 (br, H₂+H₈+H₁₁+H₁₆), 3.77-3.03 (br, H₉+H_{17,17',17''}), 1.49-1.01 (br, H₁+H₁₀+H_{18,18',18''}). **ATR-FTIR** ν_{max} cm^{-1} 3390 (br, m, -NH stretching), 2915 (s, -CH stretching), 2851 (s, -CH stretching), 2032 (w, ar), 1737 (m, ar), 1556 (s, -C=N stretching), 1450 (s), 1311 (m), 1166 (s, -CH in-plane), 1019 (m), 828 (m, ar -CH), 780 (s, ar -CH), 645 (m, -CH out-of-plane), 547 (br, m).



[VBP]Cl (**9**): $^1\text{H-NMR}$ (400 MHz, CDCl₃) δ ppm 7.36 (m, 4H, H_{4,4'}+H_{5,5'}), 6.66 (dt, $J=17.6$ Hz and $J=11.0$ Hz, 1H, H₂), 5.72 (dd, $J=17.6$ Hz and $J=2.8$ Hz, 1H, H₁), 5.25 (dd, $J=11.0$ Hz and $J=5.9$ Hz, 1H, H_{1'}), 4.27 (d, $J=15.5$ Hz, 2H, H₇), 2.38 (m, 6H, H_{8,8',8''}), 1.42 (m, 12H, H_{9,9',9'',10,10',10''}), 0.88 (t, $J=7.0$ Hz, 9H, H_{11,11',11''}). $^{13}\text{C-NMR}$ (101 MHz, CDCl₃) δ ppm 137.6 (C₃), 136.0 (C₂), 130.3 (C_{5,5'}), 130.0 (C₆), 127.0 (C_{4,4'}), 114.9 (C₁), 26.8 (C₇), 23.9 (C_{9,9',9'',10,10',10''}), 18.7 (C_{8,8',8''}), 13.6 (C_{11,11',11''}). $^{31}\text{P-NMR}$ (162 MHz, CDCl₃) δ ppm 31.7. **ATR-FTIR** ν_{max} cm^{-1} 2957 (m, -CH stretching), 2871 (s, -CH stretching), 1512 (m), 1460 (m, P-(CH₂-CH₃)₃), 1415 (m, -C-P stretching), 1379 (m, C=C), 1282 (w, P-CH₂-), 1095 (m, ring -CH in-plane), 989 (m), 910 (s, ar -CH), 856 (s, ar -CH).



P[VBP]Cl (**P5**): $^1\text{H-NMR}$ (400 MHz, $\text{DMSO-}d_6$) δ ppm 7.61-7.14 (br, $\text{H}_{4,4'}$), 6.73-6.15 (br, $\text{H}_{5,5'}$), 4.56-3.90 (br, H_7), 2.49-2.09 (br, $\text{H}_2+\text{H}_{8,8',8''}$), 1.56-1.14 (br, $\text{H}_1+\text{H}_{9,9',9'',10,10',10''}$), 0.98-0.72 (br, $\text{H}_{11,11',11''}$). $^{13}\text{C-NMR}$ (101 MHz, $\text{DMSO-}d_6$) δ ppm 144.8 (ar, $\text{C}_{5,5'}$), 130.5 (br, C_4), 128.0 (ar, C_4'), 60.2 (C_2+C_7), 57.9 ($\text{C}_{8,8',8''}$), 23.5 ($\text{C}_1+\text{C}_{9,9',9''}$), 18.0 ($\text{C}_{10,10',10''}$), 13.7 ($\text{C}_{11,11',11''}$). $^{31}\text{P-NMR}$ (162 MHz, $\text{DMSO-}d_6$) δ ppm 32.2. **ATR-FTIR** ν_{max} cm^{-1} 3371 (br, m, OH stretching, H_2O), 2929 (s, -CH stretching), 2872 (s, -CH stretching), 1733 (w, ar), 1627 (w, ar), 1511 (m), 1464 (m, $\text{P-(CH}_2\text{-CH}_3)_3$), 1238 (m), 1097 (m), 911 (m, ar -CH), 847 (m, C-H bend benzene ring), 719 (m, C-H bend benzene ring), 569 (br, m).



Phosphonium co-PIL_{50/50} (**P6**): $^1\text{H-NMR}$ (400 MHz, $\text{DMSO-}d_6$) δ ppm 8.95-8.55 (br, H_4), 8.42-8.30 (br, $\text{H}_6+\text{H}_7+\text{H}_{13,13'}$), 7.44-6.88 (br, $\text{H}_{14,14'}$), 4.71-4.19 (br, $\text{H}_2+\text{H}_8+\text{H}_{11}+\text{H}_{16}$), 3.65-3.13 (br, $\text{H}_9+\text{H}_{17,17',17''}$), 2.43-2.03 (br, $\text{H}_{18,18',18''}$), 1.61-1.22 (br, $\text{H}_1+\text{H}_{10}+\text{H}_{19,19',19''}$), 0.97-0.75 (br, $\text{H}_{20,20',20''}$). **ATR-FTIR** ν_{max} cm^{-1} 3401 (br, m, -NH stretching), 2930 (s, -CH stretching), 2872 (s, -CH stretching), 2032 (w, ar), 1650 (m, ar), 1556 (s, -C=N stretching), 1451 (s, $\text{P-(CH}_2\text{-CH}_3)_3$), 1371 (m), 1179 (s, -CH in-plane), 1096 (m), 964 (m, ar -CH), 916 (s, ar -CH), 847 (m, -CH out-of-plane), 595 (br, m).

4.1 BJH-pore size distribution and nitrogen adsorption-desorption isotherm

In Figure S.3, the lines in BJH-pore size distributions and nitrogen adsorption-desorption isotherms are only for visual guidance. Due to their similarity, only one curve is presented for exemplification.

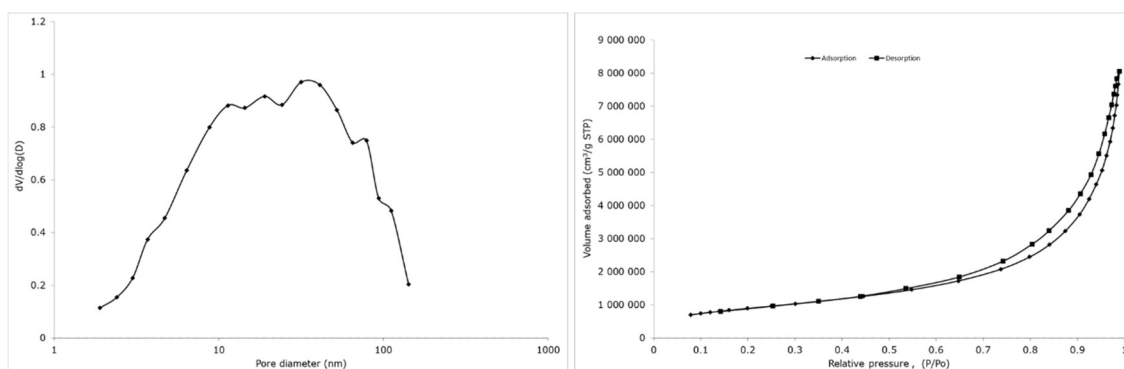


Figure S.3. BJH-pore size distribution and nitrogen adsorption-desorption isotherm for **C:E:M1:P2_{80%}**.

4.2 Elemental Analysis

Table S. 1. CHN elemental analysis of the aerogels with and without PIL and their corresponding N/C ratio.

Entry	Particles	Elements			N (%) / C (%)
		C (%)	H (%)	N (%)	
1	C	38.41	6.30	6.68	0.174
2	C:G	38.06	6.57	6.31	0.166
3	C:G:P4 _{30%}	38.63	6.15	6.72	0.174
4	C:G:P1 _{30%}	38.37	6.48	6.97	0.182
5	C:E:M4	42.26	7.05	7.39	0.175
6	C:E:M4:P2 _{30%}	41.43	7.20	6.93	0.167
7	C:E:M2:P1 _{30%}	40.69	6.92	7.88	0.194
8	C:G:P4 _{30%} reused	43.78	7.18	4.98	0.114
9	C:E:M1:P2 _{80%}	36.07	6.52	5.90	0.164

Observing Table S.1, it is possible to verify that there is no significant variation in the values, which is in agreement with the CO₂ capture capacities obtained, also very similar.

4.3 FTIR-ATR of PILs and AEROPILs

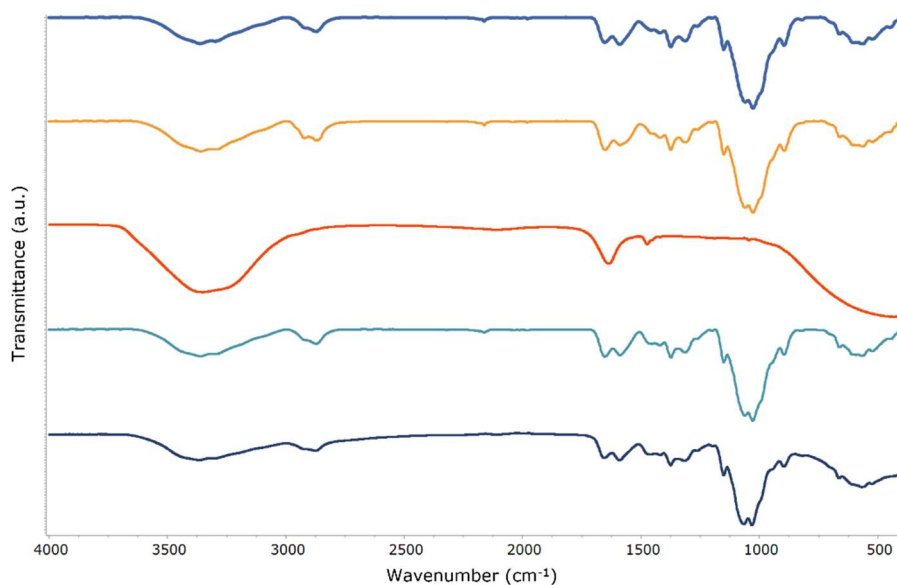


Figure S.4. ATR-IR spectra of (blue) C:M3, (orange) C:E:M4, (red) P2, (cyan) C:E:M4:P2_{30%} and (dark blue) C:E:M2:P2_{30%}.

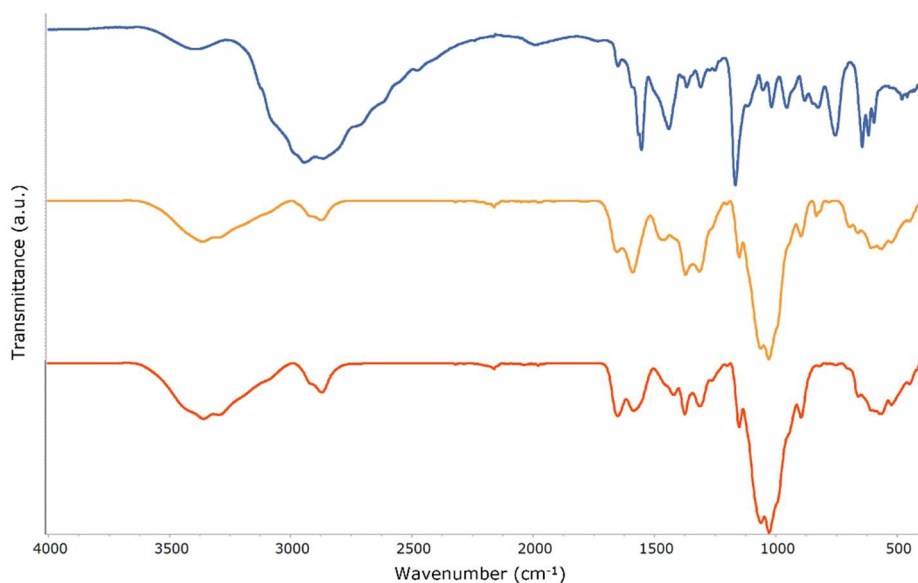


Figure S.5. ATR-IR spectra of (blue) **P1**, (orange) **C:G:P1_{30%}** and (red) **C:E:M2:P1_{30%}**.

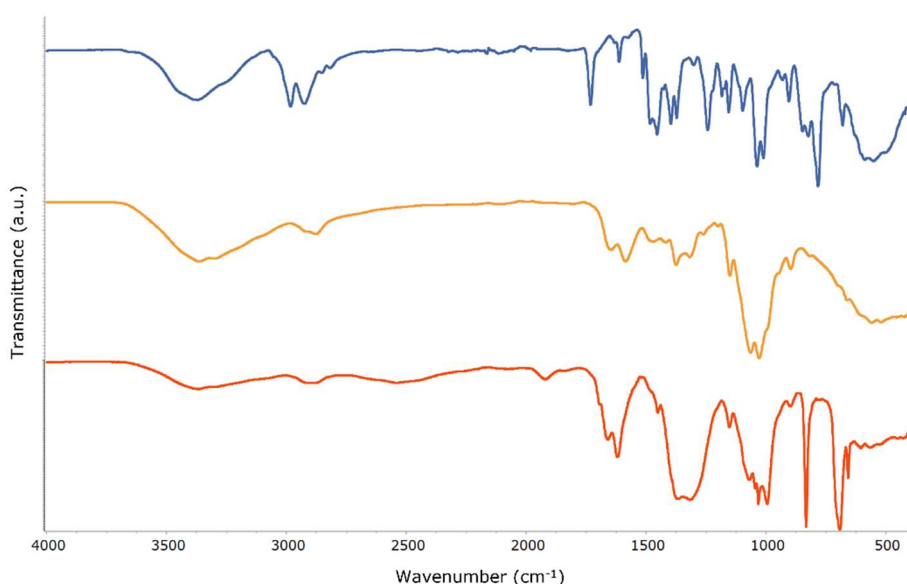


Figure S.6. ATR-IR spectra of (blue) **P3**, (orange) **C:G** and (red) **C:G:P3_{30%}**.

4.4 TGA curves

Overall, at temperatures up to around 200 °C, there is the release of H₂O due to dehydration and/or dehydroxylation, with the mass loss for chitosan (C) beads being lower than for most *AEROPILs*. The significant mass loss occurs above 200 °C and up to around 400 °C, while between 400 °C and 800 °C there is no abrupt mass loss but a continuous mass decrease for C beads and all *AEROPILs*. The mass loss between 200 and 800 °C is lower for *AEROPILs* than for C beads. In general, the TGA profiles of the *AEROPILs* are qualitatively similar to that of C beads, indicating that the PILs are incorporated in the structure.

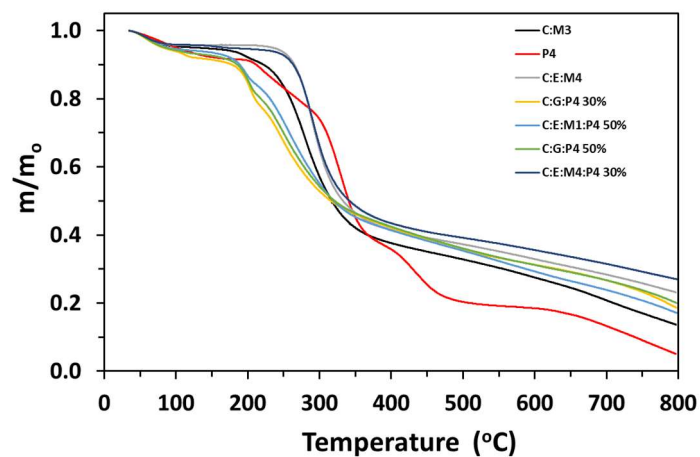


Figure S.7. TGA thermograms of C aerogel beads, co-PIL (P4) and AEROPILs with P4 (m_0 is the mass at 35 °C).

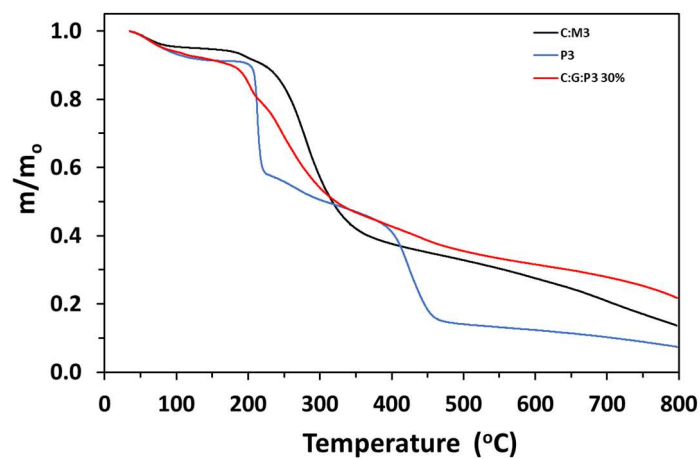


Figure S.8. TGA thermograms of C aerogel beads, P[VBA]Cl (P3) and AEROPILs with P3 (m_0 is the mass at 35 °C).

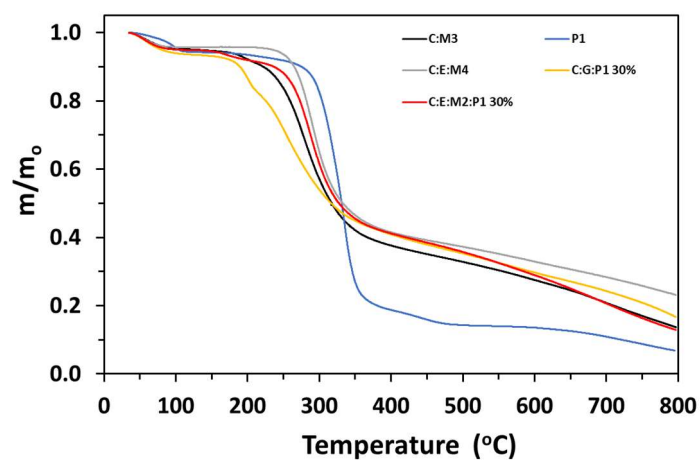


Figure S.9. TGA thermograms of C aerogel beads, P[AEIM]Br.HBr (P1) and AEROPILs with P1 (m_0 is the mass at 35 °C).

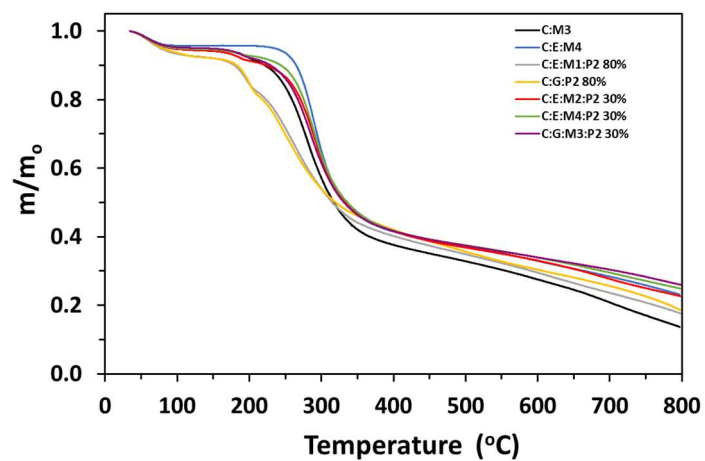


Figure S.10. TGA thermograms of C aerogel beads and *AEROPILs* with P[DADMA]Cl (**P2**) (m_0 is the mass at 35 °C).

4.5 Solid-state NMR analysis

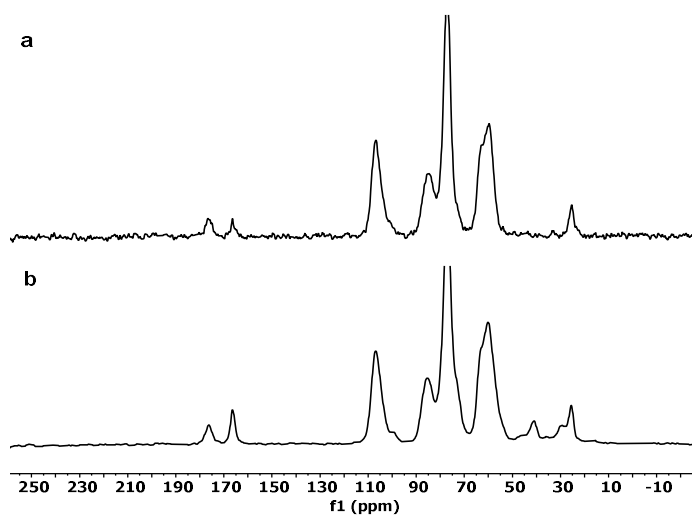


Figure S.11. ^{13}C CP-TOSS NMR spectra of (a) C and (b) C:E:M1:P2_{80%} beads.

5 Supercritical drying apparatus from Paralab

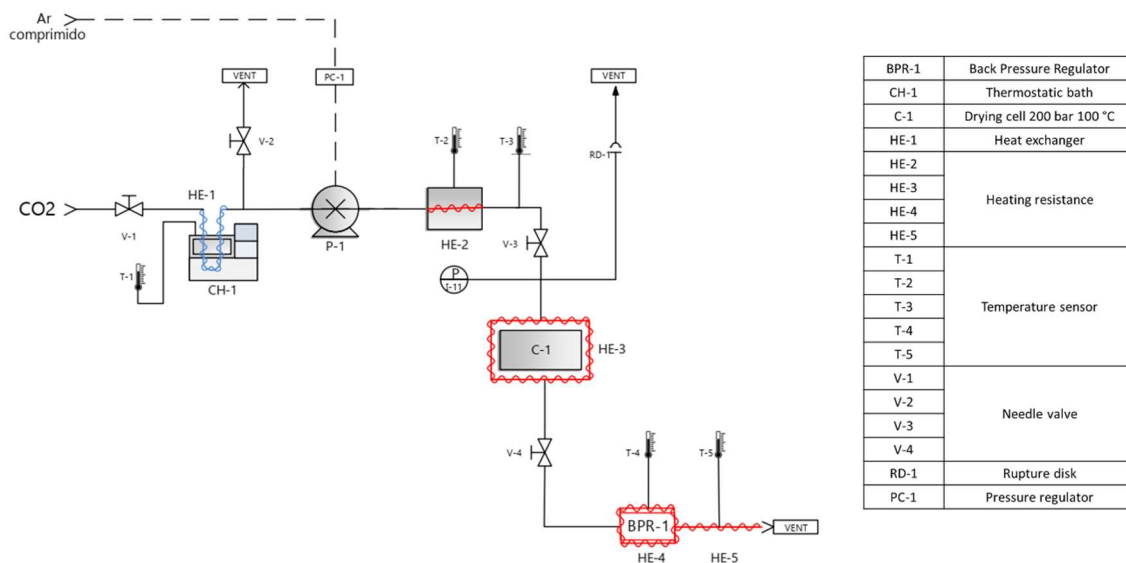


Figure S.12. Costumed-made supercritical drying apparatus from Paralab.

6 Morphological and textural properties of the chitosan aerogels

A library of stable chitosan aerogels with different PILs was obtained. The presence of crosslinker and heating during the preparation were also assessed, as the general approach of the *AEROPILs* preparation procedure depicted in Figure S.13.

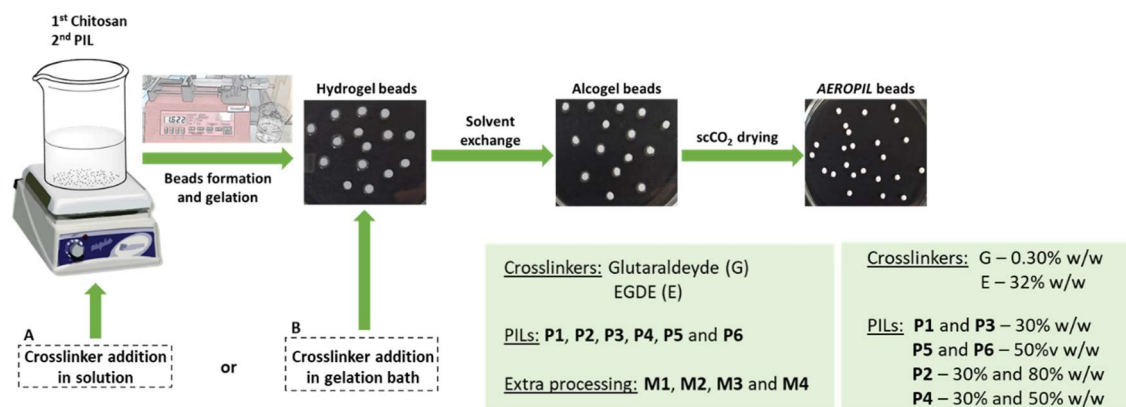


Figure S.13. General scheme of the next *AEROPIL* beads preparation procedure.

In addition, the physicochemical (Table S.2) and textural properties (Table S.3) of the *AEROPILs* were studied. Regarding the physicochemical properties, it is possible to observe that when beads are heated, there is only a slight decrease in ρ_{env} (Table S.2, entries 4, 5, 14). So, there is no apparent advantage in introducing this heating step; moreover, the beads become more stable and uniform without heating.

The incorporation of a higher amount of PIL in the aerogel (Table S.2, entries 6, 8, 11, 16) led to an increase in the ρ_{env} and a slight decrease of the overall porosity, which is compatible with some pore-filling effect from the PIL. This effect must be further assessed regarding the final application since porosity control is necessary but not a determining factor [8].

Comparing the beads obtained with EGDE and glutaraldehyde (Table S.2, entries 2-11 and 12-17, respectively), there were no significant differences between glutaraldehyde and an aqueous EGDE solution. However, significant differences were observed if EGDE was directly incorporated in the chitosan solution, as the ρ_{env} was enhanced and the overall porosity and diameter diminished.

The skeletal densities of the chitosan/PIL aerogels without glutaraldehyde were determined using helium pycnometry. These densities were lower compared to the ρ_{skel} of pure chitosan ($1.414 \pm 0.030 \text{ g/cm}^3$ [9]). This divergence might be attributed to the influence of PIL, which likely prompts the formation of smaller pores that helium molecules cannot access [10].

Table S.2. Influence of PILs, crosslinker and heating of the chitosan gel beads on the physicochemical properties of the resulting chitosan aerogel particles. Notation: ρ_{skel} , skeletal density (measured by helium pycnometry); ρ_{env} , envelope density; ϵ , overall porosity.

Entry	Particles	Diameter (mm)	ρ_{skel} (g/cm ³)	ρ_{env} (g/cm ³)	ϵ (%)	Overall volume shrinkage (%)
1	C:M3	3.97 (0.1)	1.272 (0.007)	0.038 (0.006)	97.0 (0.5)	42.9 (11.2)
2	C:E:M4	3.68 (0.1)	1.403 (0.006)	0.047 (0.009)	96.6 (0.6)	55.2 (9.2)
3	C:E:M1	2.92 (0.1)	1.502 (0.009)	0.103 (0.022)	93.2 (1.5)	72.2 (6.8)
4	C:E:M2:P2 _{30%}	3.51 (0.1)	1.368 (0.001)	0.046 (0.009)	96.7 (0.7)	59.7 (8.6)
5	C:E:M4:P2 _{30%}	3.82 (0.1)	1.411 (0.002)	0.037 (0.007)	97.4 (0.5)	53.5 (9.3)
6	C:E:M1:P2 _{30%}	2.79 (0.1)	1.334 (0.006)	0.110 (0.025)	91.8 (1.9)	77.8 (5.6)
7	C:E:M4:P4 _{30%}	3.52 (0.1)	1.388 (0.010)	0.053 (0.010)	96.2 (0.7)	72.2 (5.7)
8	C:E:M1:P4 _{50%}	2.42 (0.2)	1.314 (0.005)	0.156 (0.041)	88.1 (3.1)	86.4 (3.8)
9	C:E:M2:P1 _{30%}	3.52 (0.1)	1.286 (0.018)	0.057 (0.011)	95.6 (0.8)	74.0 (5.2)
10	C:E:M1:P5 _{50%}	3.42 (0.1)	1.445 (0.010)	0.056 (0.011)	96.2 (0.8)	68.7 (6.6)
11	C:E:M1:P6 _{50%}	3.03 (0.1)	1.437 (0.007)	0.097 (0.020)	93.2 (1.4)	68.8 (7.5)
12	C:G:P4 _{30%}	3.68 (0.1)	1.441 (0.000)	0.050 (0.009)	96.5 (0.6)	71.4 (5.6)
13	C:G:P1 _{30%}	3.85 (0.1)	1.406 (0.007)	0.047 (0.008)	96.7 (0.6)	67.0 (6.2)
14	C:G:M3:P2 _{30%}	4.02 (0.1)	1.270 (0.006)	0.035 (0.006)	97.3 (0.5)	61.5 (7.1)
15	C:G:P4 _{50%}	3.68 (0.1)	1.486 (0.010)	0.043 (0.008)	97.1 (0.5)	27.6 (15.9)
16	C:G:P2 _{80%}	3.41 (0.1)	1.428 (0.006)	0.060 (0.012)	95.8 (0.8)	68.2 (6.8)
17	C:G:P3 _{30%}	3.10 (0.1)	1.426 (0.007)	0.078 (0.016)	94.5 (1.2)	75.4 (5.6)

Standard deviation was calculated using measurements of minimum *ca.* 14 aerogel beads.

The textural properties (a_{BET} , $V_{p,BJH}$ and $D_{p,BJH}$) of PIL-chitosan aerogel particles were obtained by nitrogen adsorption-desorption analysis (Table S.3). In the case of **P4**, there is a higher percentage of mesopores relative to the other formulations, especially in higher PIL content (Table S.3, entries 8, 15). The remaining cases are quite homogeneous, except for **P1**, which diminished the specific surface area when EGDE was used as a crosslinker (Table S.3, entry 9 and 13). Moreover, the heating step did not induce significant changes to the beads. The relative contribution of the mesopore and macropore volumes to the total pore volume (V_{mes} , V_{MP} , $V_{p,meso}$ and $V_{p,macro}$ in Table S.3, respectively) unveiled that the V_{MP} was predominant (above 72.6% in all cases). The dual porosity is relevant since macropores enhance CO₂ diffusion and accessibility of active sites by guest molecules, and mesopores provide size and shape selectivity [8]. Interestingly, $V_{p,meso}$ was usually between 2.9 and 9.9%, except when higher **P2** and **P4** percentages were used (Table S.3, entries 6, 8, 15).

Table S.3. Textural properties evaluated by nitrogen adsorption-desorption tests of the chitosan aerogel particles. Notation: a_{BET} , specific surface area by the BET method; $V_{\text{P,BJH}}$, overall specific pore volume obtained by the BJH method; V_{mes} , specific mesopore volume; V_{MP} , specific macropore volume; $D_{\text{P,BJH}}$, mean pore diameter by the BJH method.

Entry	Particles	a_{BET} (m^2/g)	$V_{\text{P,BJH}}$ (cm^3/g)	$D_{\text{P,BJH}}$ (nm)	V_{mes} (cm^3/g)	V_{MP} (cm^3/g)	$V_{\text{p,meso}}$ (%)	$V_{\text{p,macro}}$ (%)
1	C:M3	323 (16)	1.37 (0.07)	14.5 (0.7)	0.97 (0.05)	24.84 (3.90)	3.8	96.2
2	C:E:M4	318 (16)	1.27 (0.06)	14.0 (0.7)	0.91 (0.05)	19.59 (3.05)	4.4	95.6
3	C:E:M1	173 (9)	0.90 (0.04)	18.3 (0.9)	0.61 (0.03)	8.48 (1.38)	6.7	93.3
4	C:E:M2:P2 _{30%}	285 (14)	1.10 (0.05)	13.2 (0.7)	0.79 (0.04)	20.44 (3.58)	3.7	96.3
5	C:E:M4:P2 _{30%}	266 (13)	1.30 (0.06)	16.6 (0.8)	0.79 (0.04)	25.74 (5.04)	3.0	97.0
6	C:E:M1:P2 _{80%}	330 (17)	1.26 (0.06)	12.3 (0.6)	0.95 (0.05)	7.43 (1.04)	11.4	88.6
7	C:E:M4:P4 _{30%}	294 (15)	1.35 (0.07)	15.4 (0.8)	0.96 (0.05)	17.18 (2.33)	5.3	94.7
8	C:E:M1:P4 _{50%}	488 (24)	2.00 (0.10)	13.7 (0.7)	1.54 (0.08)	4.09 (0.81)	27.4	72.6
9	C:E:M2:P1 _{30%}	185 (9)	0.96 (0.05)	17.3 (0.9)	0.63 (0.03)	16.19 (6.35)	3.8	96.3
10	C:E:M1:P5 _{30%}	287 (14)	1.09 (0.05)	12.9 (0.6)	0.90 (0.04)	16.41 (2.37)	5.2	94.8
11	C:E:M1:P6 _{50%}	269 (13)	1.20 (0.06)	14.8 (0.7)	0.95 (0.05)	8.63 (1.30)	9.9	90.1
12	C:G:P4 _{30%}	203 (10)	0.87 (0.04)	14.4 (0.7)	0.63 (0.03)	18.71 (2.17)	3.3	96.7
13	C:G:P1 _{30%}	183 (9)	0.83 (0.04)	15.4 (0.8)	0.59 (0.03)	20.10 (2.32)	2.9	97.2
14	C:G:M3:P2 _{30%}	387 (19)	1.83 (0.09)	15.8 (0.8)	1.20 (0.06)	26.72 (4.76)	4.3	95.7
15	C:G:P4 _{50%}	748 (37)	3.71 (0.19)	16.8 (0.8)	2.54 (0.13)	20.13 (2.30)	11.2	88.8
16	C:G:P2 _{80%}	258 (13)	1.15 (0.06)	14.5 (0.7)	0.81 (0.04)	15.18 (1.76)	5.1	94.9
17	C:G:P3 _{30%}	301 (15)	1.35 (0.07)	15.0 (0.7)	0.97 (0.05)	11.07 (1.49)	8.1	91.9

7 CO₂ capture

The adsorption-desorption behaviour of CO₂ on aerogels was assessed after heating under helium at 120 °C. The aerogels did not decompose at this temperature, as shown by the TGA curves in Section 4.4 in Supporting Information. CO₂ adsorption-desorption results at 25 °C, and a pressure of 1 bar are presented in Figure S.14, showing that the materials could adsorb and retain CO₂. When the gas was switched from helium to CO₂, adsorption was initially rapid but then increased gradually. A plateau was not reached after exposure to a flow of 100 mL min⁻¹ of CO₂ for 10 min, indicating that higher adsorbed CO₂ amounts would be obtained with a longer exposure time.

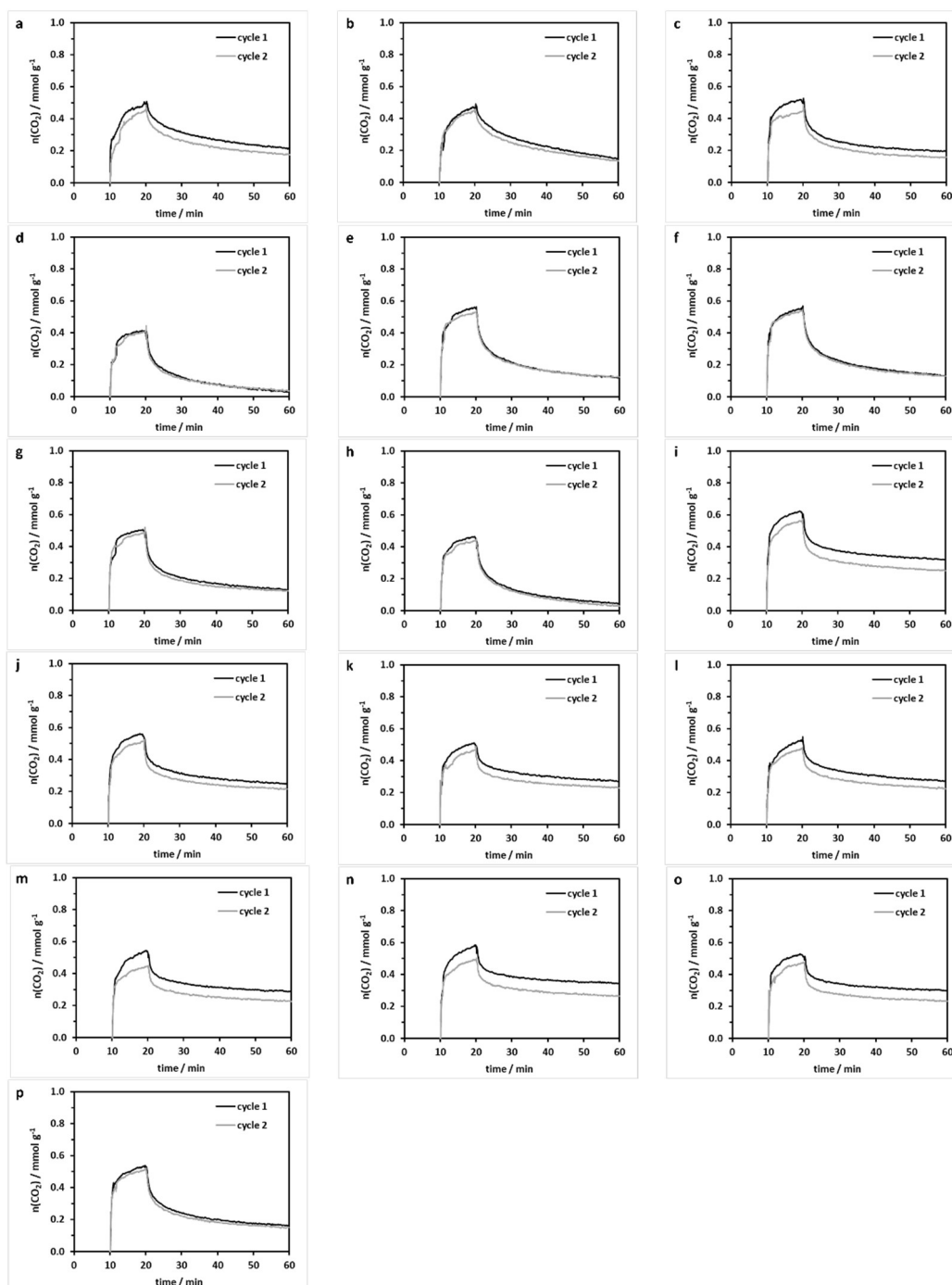


Figure S.14. Adsorption-desorption of CO₂, at 25 °C and 1 bar, on (a) C, (b) C:G, (c) C:M3, (d) C:E:M4, (e) C:E:M2:P1_{30%}, (f) C:E:M2:P2_{30%}, (g) C:E:M4:P2_{30%}, (h) C:E:M4:P4_{30%}, (i) C:E:M1:P2_{80%}, (j) C:E:M1:P4_{50%}, (k) C:G:P4_{30%}, (l) C:G:P1_{30%}, (m) C:G:P4_{50%}, (n) C:G:P2_{80%}, (o) C:G:P3_{30%}, and (p) C:G:M3:P2_{30%} aerogel beads.

All these features are similar to those obtained in our previous work [9]. Adsorption capacities are of similar order of magnitude as can be seen in Figure S.15. After exposure to CO₂ for 10 min, the maximum CO₂ adsorption obtained was 0.62 mmol g⁻¹ for C:E:M1:P2_{80%} which, although slightly lower than the maximum obtained with another *AEROPIL* in our previous work [9], corresponds to 31 times increase when compared with pure chitosan (0.02 mmol g⁻¹) [11]. Compared to other porous PILs, such as those described by Eftaiha et al. (0.59 mmol g⁻¹ at 25 °C and 1 bar), our present *AEROPILs* show comparable CO₂ sorption capacity [12]. The optimal adsorption of CO₂ was achieved using *AEROPIL* beads made with commercial PIL **P2**

(**C:G:P2_{80%}** and **C:E:M1:P2_{80%}**), without the need for further synthetic steps, which is interesting from the industrial point of view. In general, there is an increase in the samples with PIL and crosslinker EGDE compared to the initial one with EGDE only. Similar conclusions can be drawn regarding the set of materials with crosslinker glutaraldehyde.

Efforts to establish a correlation between the CC performance of *AEROPILs* and their textural features proved to be complex since these properties were found to affect the CC capacity non-linearly. For example, the a_{BET} values for almost all the materials were in the range from 183 to 387 $m^2 g^{-1}$, except for **C:E:M1:P4_{50%}** and **C:G:P4_{50%}** with 488 $m^2 g^{-1}$ and 748 $m^2 g^{-1}$, respectively, which does not translate in a better CC performance. Nevertheless, as seen in our previous work [9], the increase in the specific surface area and porosity achieved by 3D morphology is a positive factor that leads to an increase in the CC capacity for all the materials in the form of beads compared with pure chitosan.

Analogously to our previous work [9], after the first sorption cycle, the materials were re-heated to 120 °C, and the second sorption cycle had a profile broadly similar to that of the first, showing that the materials were able to retain most of the CO₂ for a long period. This is relevant for the catalytic application since CO₂ must remain long enough for the reaction. Furthermore, in some cases, the amounts adsorbed were the same as in the first cycle, while in most cases, the amounts adsorbed were slightly lower in the second cycle. However, the materials still adsorbed reasonable amounts of CO₂.

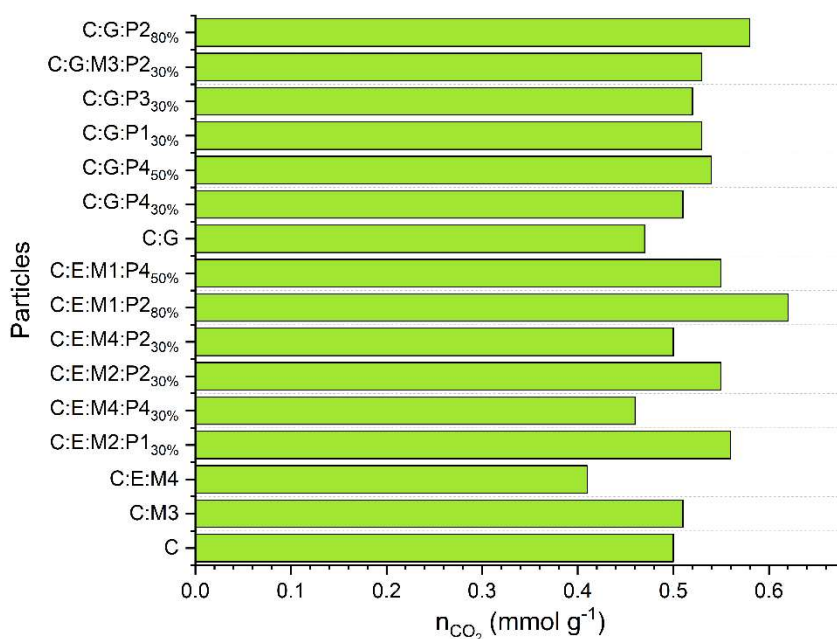


Figure S.15. CO₂ capture capacities of *AEROPILs* at 25 °C and 1 bar after exposure to CO₂ for 10 min. Notation: n_{CO_2} , CO₂ capture capacity. Errors in the measurements are estimated to be $\pm 1\%$.

8 Catalysis

8.1 GC-MS Analysis

GC Agilent 7890 GC (Palo Alto, California, USA) equipped with a split/splitless injector was used with an Agilent HP-5 MS UI fused silica capillary column (30 m x 0.25 mm i.d. x 0.25 μm df - film thickness), with a program temperature beginning in 50 °C (1 min) and going until 310

°C at a rate of 10 °C min⁻¹ (1 min). 1 μL sample volume was injected at 250 °C (split ratio set to 1:60). The carrier gas was helium (Alphagaz 99.9999%) at a constant flow rate of 1 mL min⁻¹. A Leco Pegasus® BT GC-TOFMS (LECO Corp., Saint Joseph, MI, USA) was used for GC-MS analysis. The transfer line was set at 300 °C, source 250 °C. The MS was operated in electron ionisation mode (70 eV) using a range of *m/z* 40-550. Data was processed using the software ChromaTof v5.40.12.0 (LECO Corp., Saint Joseph, MI, USA). NIST MS Search Program Version 2.3 was used for spectra matching (NIST, 2015).

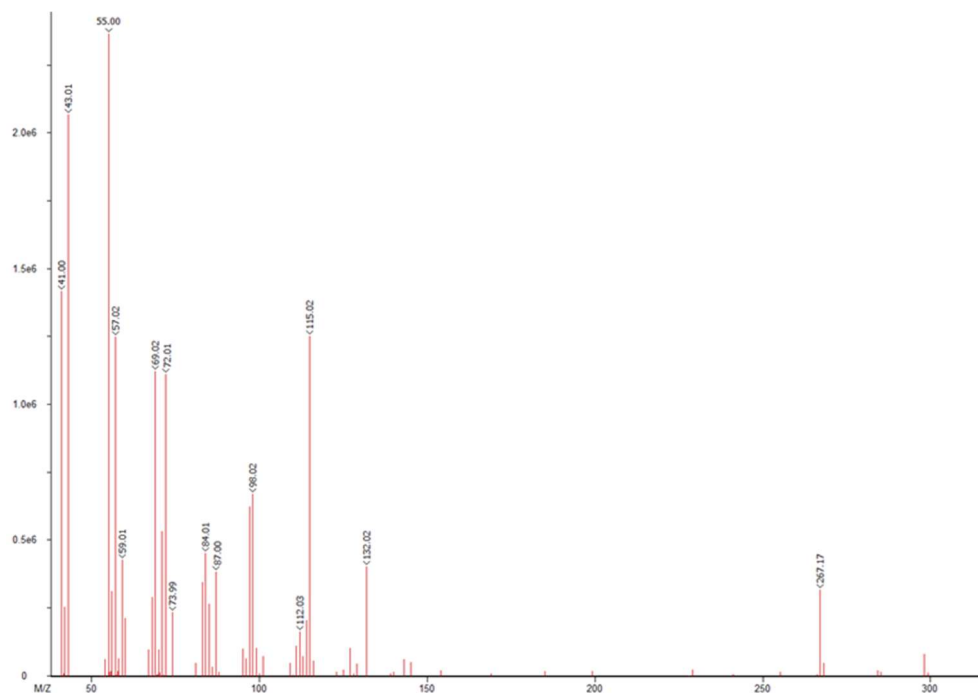


Figure S.16. ESI(+)-MS of the catalytic reaction with the C:G:P4_{50%} beads detected via GC-MS analysis ($M^{+} \approx 300$).

Table S. 4. Chemical structures of possible oligoether carbonates as side products of catalytic reactions.

<i>m/z</i>	Structures	Ref.
220		[13,14]
132		[13]
116		[15]
88		[13]

8.2 NMR spectra

The calculation of the conversion of the reaction in batch was based on the moles of epoxide, diol, and cyclic carbonate obtained from the integration of signals **a**, **b**, and **c** of the ^1H NMR spectra (an example is given in Figure S.17). The same rationale was applied to flow reactions but using styrene as an internal standard. The following equations were applied:

- (1) *mol of reaction products = mol of cyclic carbonate + mol of diol (if present)*
- (2) *conversion % = [mol of reaction products/(mol of reaction products + mol of unreacted epoxide)] x 100*
- (3) *selectivity % = (mol of cyclic carbonate/mol of reaction products) x 100*

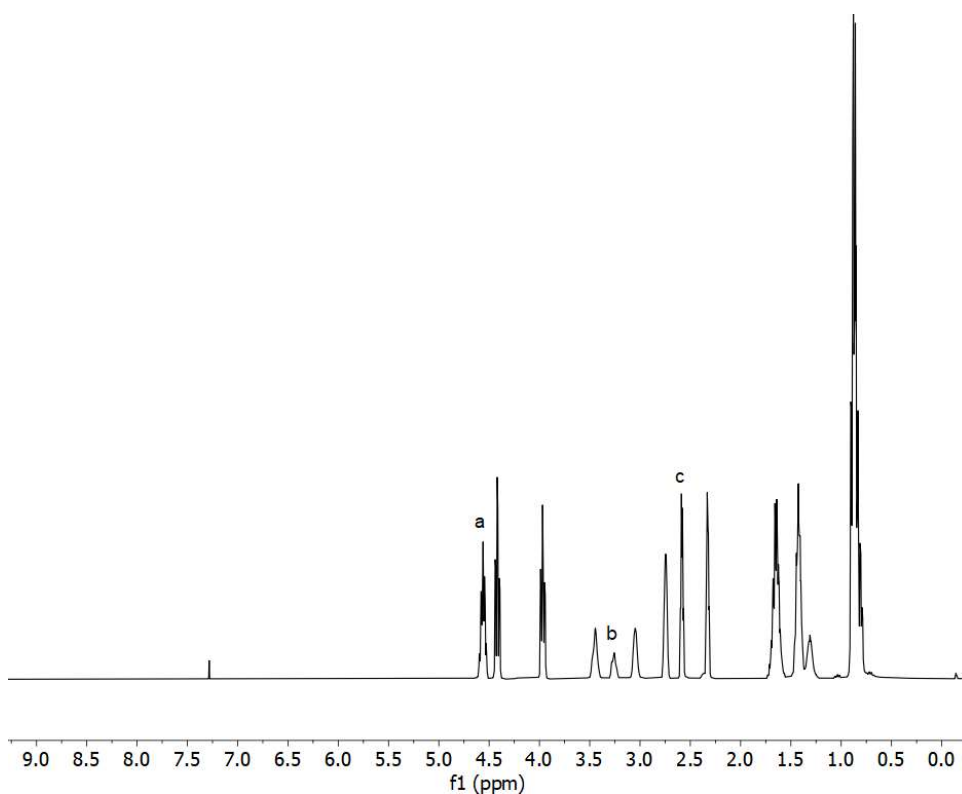


Figure S.17. ^1H -NMR (CDCl_3) spectrum of 72 h catalysis of **C:E:M1:P2**_{80%} with butylene oxide (Table 1, entry 10). (a) corresponds to cyclic carbonate, (b) corresponds to diol, and (c) corresponds to epoxide (these signals are integrated, and the respective values are used to calculate the conversion and selectivity of the reaction according to equations (1)-(3)).

Table S. 5. Comparison of CO₂ catalytic capacities and respective specific surface areas reported for different IL/PIL-based porous catalysts. The reported values are all for catalytic reactions without solvent or co-catalyst. Entries in bold correspond to results from this work.

Entry	Catalyst	BET (m ² g ⁻¹)	Substrate	t (h)	T (°C)	P (bar)	Yield (%)	Select. (%)	Ref.
1	COF-IL	291.0	Styrene oxide	48	80	1	98.0	nd	[16]
2	Aerogel COF-IL@chitosan	103.3		72			91.0	nd	
3	Ch-ILBr	57.0		5	120	20	96.0	100	
4	ImIP@TT-COF	46.0	Styrene oxide	48	120	1	> 99.0	> 99	[18]
5	MIL-101-NHIM-NH ₂	441.0	Butylene oxide	4	120	20	88.7	nd	[19]
			Styrene oxide				66.7	nd	
6	PPIL@COF ^A -40	134.0	Butylene oxide	48	100	20	94	nd	[20]
			Styrene oxide	60			93		
7	PIL-MCOF-320-10-100	174.0	Butylene oxide	36	90	10	96.0	nd	[21]
			Styrene oxide				95.0		
8	COF-TpPa-Py-Br ⁻	113.0	Epichlorohydrin	18	100	1	> 99.0	nd	[22]
			Glycidyl Phenyl Ether				10.0		
9	COF-HNU14	196.0	Butylene oxide	36	120	20	95.0	nd	[23]
10	COF-HNU3	2027.0	Butylene oxide	48	100	20	95.0	nd	[24]
			Styrene oxide	72			94.0		
11	C:G:P₄30%	203.0	Butylene oxide	72	135	10	77	88	This work
12	C:G:P₄30%		Epichlorohydrin				81	90	This work
13	C:E:M₁:P₂80% (pre-treated)		Butylene oxide				68	91	This work

8.3 Catalyst Regeneration

Encouraged by these promising findings and with the established optimal conditions, subsequent investigations were undertaken to explore the regeneration of *AEROPILs* and take full advantage of having a heterogeneous catalyst. The ability to reuse the catalyst beads was preliminary evaluated through solvent screening while controlling the total bead size reduction (Table S.6).

Table S. 6. Measurements from digital camera analysis of the chitosan aerogel particles subjected to a solvent screening to access aerogel particles integrity with the corresponding total size reduction.

Entry	Time	Original (mm ²)	Ethanol	Methanol	Diethyl Ether	Acetonitrile	Acetone	Dichloromethane	Ethyl acetate
1 ^a	29 h	8.066	8.086	9.624	4.606	7.942	6.068	6.861	9.016
2 ^a	31 h	10.515	2.994	2.984	6.047	2.550	2.604	4.789	2.461
3 ^b	7 days ^d	26.336	23.129	26.357	18.364	18.525	12.609	15.096	25.913
4 ^b	5 h ^e	19.233	5.581	5.728	9.267	5.319	5.876	9.361	5.823
5 ^b	2 days ^d	11.440	3.384	3.533	5.618	2.980	3.096	5.328	3.304
TOTAL^c	-----	56%	85%	86%	69%	84%	75%	65%	87%

^a Preliminary measurement with 1 aerogel particle. ^b Measurements with an average of 4 aerogel particles. ^c Total size reduction (in percentage) of the aerogel particles after drying for 2 days, comparing to the original size after 7 days in the solvent or open air for the original column beads. ^d Amount of time in solvent or open air. ^e Amount of time in ambient pressure drying.

This screening was essential to establish a washing protocol to maintain the bead's integrity. The washing was performed with ethanol, methanol, diethyl ether, acetonitrile, acetone, dichloromethane, or ethyl acetate followed by subsequent drying. The results herein presented are related to ambient pressure drying, simplifying the process and avoiding a scCO₂ drying step each time a catalytic reaction is made. Diethyl ether and dichloromethane induced a lower reduction in the bead size. However, as dichloromethane is a chlorinated solvent, diethyl ether was selected for further analysis.

Besides the ambient pressure drying, a second supercritical drying was tested in the case of ethanol. The textural properties (a_{BET} , $V_{\text{P,BJH}}$, $D_{\text{P,BJH}}$ and V_{mes}) of the aerogel particles subjected to a second scCO_2 drying (ethanol) and an ambient pressure drying (diethyl ether) obtained by nitrogen adsorption-desorption analysis are presented in Table S.7. As it is possible to verify, there was a decrease of the textural properties for the beads subjected to a second scCO_2 drying, except for $D_{\text{P,BJH}}$.

Table S. 7. Textural properties evaluated by nitrogen adsorption-desorption of the chitosan aerogel particles subjected to recyclability tests. Notation: a_{BET} , specific surface area by the BET method; $V_{\text{P,BJH}}$, overall specific pore volume obtained by the BJH method; V_{mes} , specific mesopore volume; $D_{\text{P,BJH}}$, mean pore diameter by the BJH method.

Particles	a_{BET} (m^2/g)	$V_{\text{P,BJH}}$ (cm^3/g)	$D_{\text{P,BJH}}$ (nm)	V_{mes} (cm^3/g)
C:G	363 (18)	1.47 (0.07)	13.8 (0.7)	1.14 (0.06)
C:G (EtOH)	254 (13)	1.23 (0.06)	16.5 (0.8)	0.85 (0.04)
C:G (ether)	177 (9)	0.81 (0.04)	16.2 (0.8)	0.59 (0.03)

In the first attempts of regeneration of the *AEROPILs* after the catalytic reactions, the beads were completely rinsed with diethyl ether and subjected to ambient pressure drying for the next catalytic cycle under the same reaction conditions. Table S.8 shows an example of a catalytic reaction with reuse afterwards.

Table S. 8. CO_2 cycloaddition catalysed by *AEROPILs* in the absence of co-catalyst and solvent and subsequent regeneration.^{a,b}

Catalyst	Conversion (%)	Selectivity (%)
C:G:P4 _{30%}	94	44
C:G:P4 _{30%} (1 st reuse)	6	99

^a Reactions carried out at 135 °C and 10 bar of pressure for 72 h using 100 mg of catalyst and 100 mg of butylene oxide. ^b Conversion determined by ^1H NMR spectroscopy on the reaction mixture with CDCl_3 .

There is an abrupt reduction of the conversion capacity, which can be an indication either of the loss of active sites for the reaction to occur due to the entrapment of cyclic carbonate, PIL lixiviation, or loss of the morphology appropriate for the reaction to occur, or even a combination of several of these factors.

From Figure S.18, it is possible to see that the morphology at the bead's surface is entirely different from what was seen in Figure 2 (D), which can block the entrance of the epoxide and CO_2 into the bead, explaining the reduced catalytic activity. Also, the EDS of the reused beads showed that nitrogen is still present and can be from two different sources, chitosan and PIL. The presence of sodium, which can only come from the coagulation bath of the beads, is detected. This is a breakthrough in understanding the process of hydrogel to aerogel transformation since this detail has never been mentioned to the best of our knowledge.

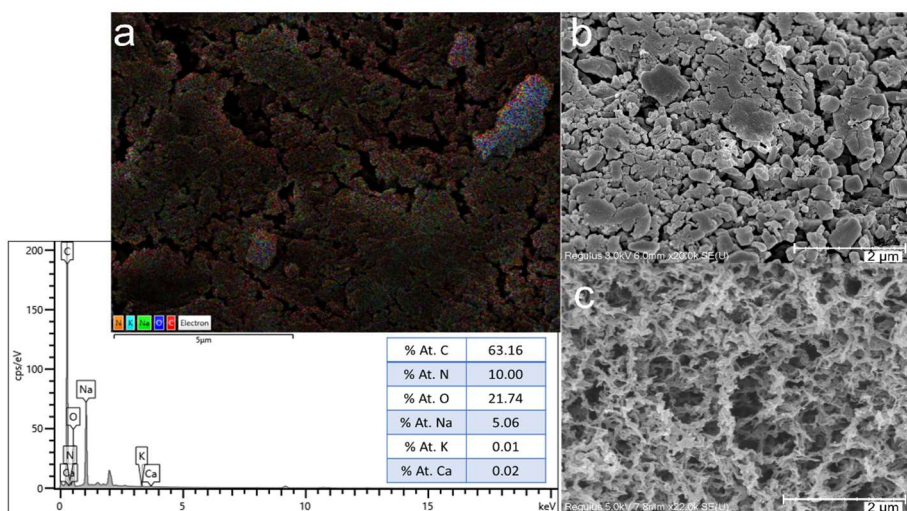


Figure S.18. (a) EDS map of a cross-section of the bead C:G:P₄₃₀% (1st reuse). Textural appearance of the (b) surface of beads C:G:P₄₃₀% (1st reuse), and (c) interior of beads C:G:P₄₃₀% (1st reuse), by SEM imaging (scale bar: 2 μ m).

¹³C CP-TOSS NMR spectra (Figure S.19) confirm that for these beads, the cyclic carbonate stayed entrapped inside; therefore, the final catalytic conversion does not reflect the real conversion percentage that will be superior, and the reduced catalytic activity in the 2nd cycle is explained.

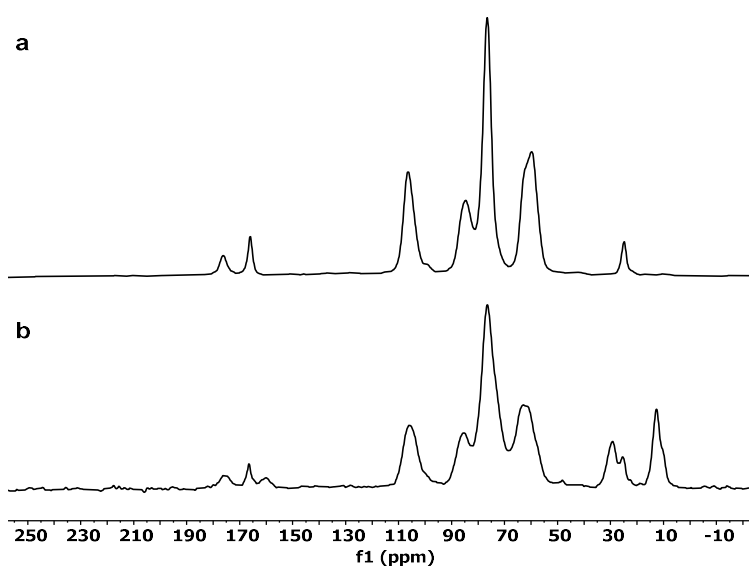


Figure S.19. ¹³C CP-TOSS NMR spectra of (a) C:G:P₄₃₀% before catalysis and (b) C:G:P₄₃₀% reused beads.

After these first attempts, the regeneration protocol for *AEROPIL* beads was set.

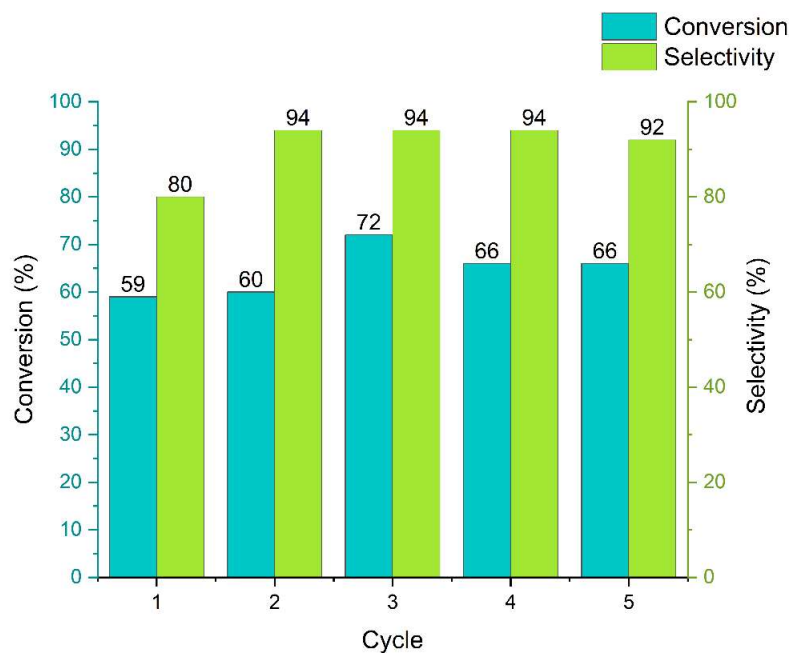


Figure S.20. CO₂ cycloaddition catalysed by *AEROPIL* C:E:M1:P2_{80%} without co-catalyst and solvent with subsequent regeneration. Reactions carried out at 135 °C and 10 bar of pressure for 72 h using 100 mg of catalyst and 11.5 mmol of butylene oxide. Conversion determined by ¹H NMR spectroscopy on the reaction mixture with CDCl₃.

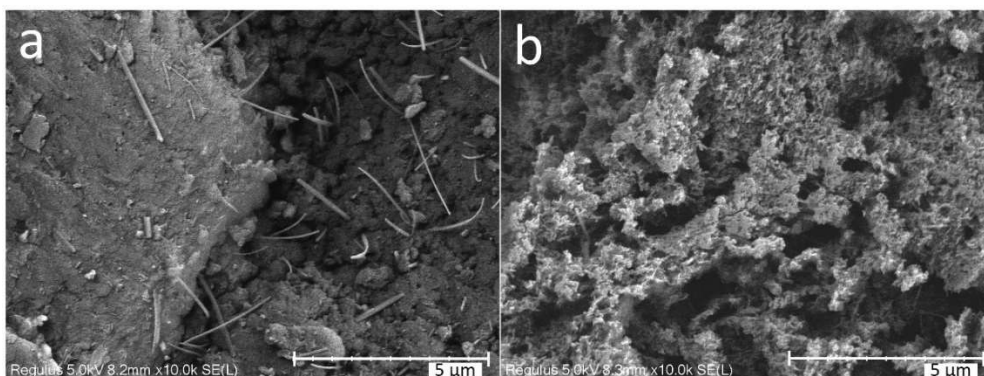


Figure S.21. Textural appearance of the (a) surface of beads C:E:M1:P2_{80%} (after 5th cycle), and (b) interior of beads C:E:M1:P2_{80%} (after 5th cycle), by SEM imaging (scale bar: 5 μm).

8.4 Continuous flow CO₂ cycloaddition

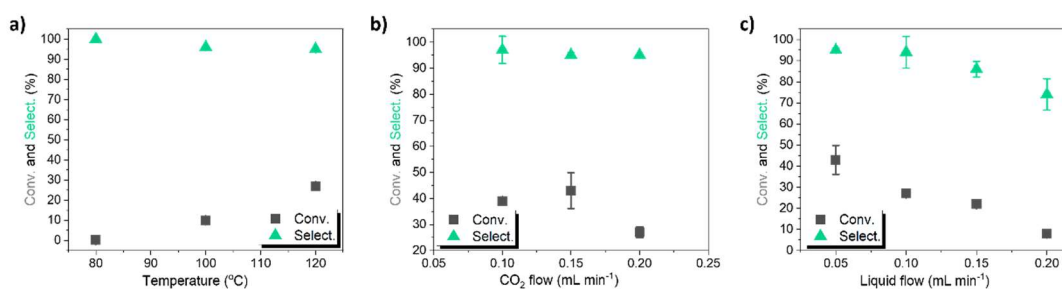


Figure S.22. (a) Temperature variation, 0.20 mL min⁻¹ CO₂ flow and 0.05 mL min⁻¹ liquid flow. (b) CO₂ flow variation, 120 °C and 0.05 mL min⁻¹ liquid flow. (c) Liquid flow variation, 120 °C and 0.15 mL min⁻¹ CO₂ flow.

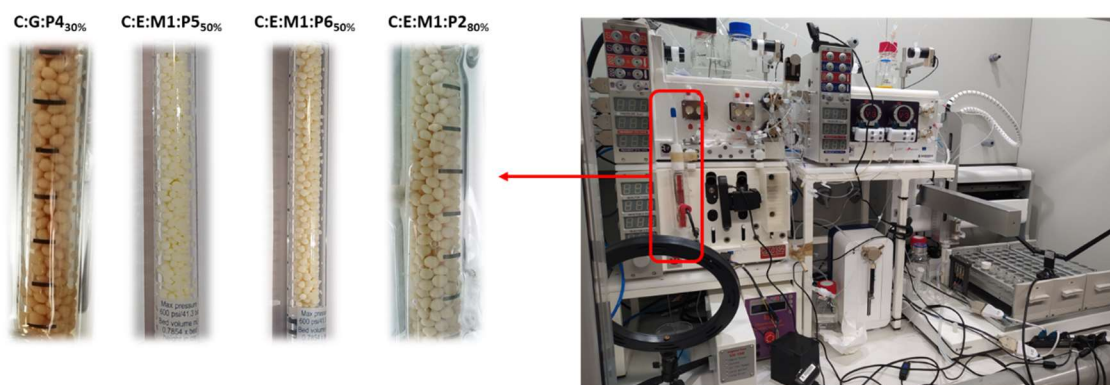


Figure S.23. Vapourtec continuous flow system and the respective *AEROPIL* catalysts after CO₂ cycloaddition reactions – C:E:M1:P2_{80%}, C:E:M1:P6_{50%}, C:E:M1:P5_{50%} and C:G:P4_{30%}.

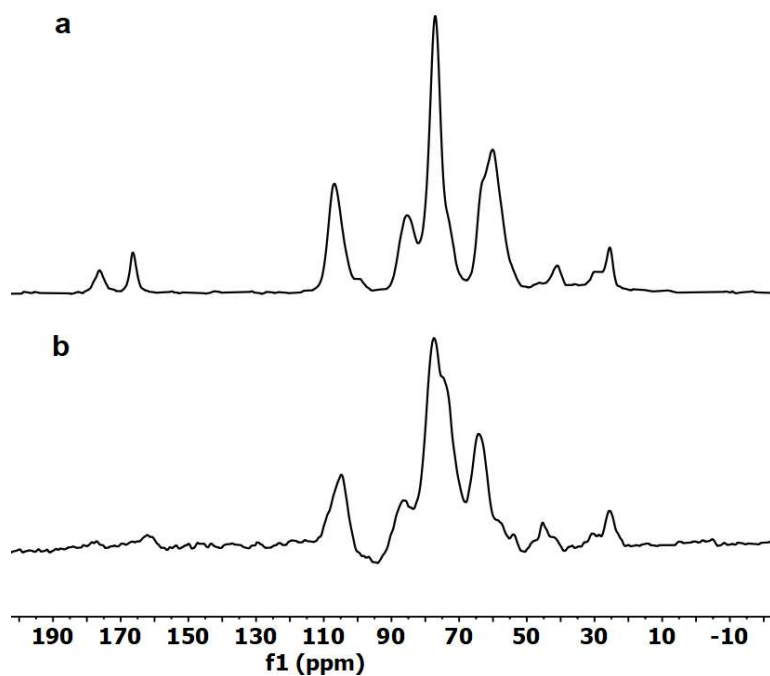


Figure S.24. (a) ¹³C CP-TOSS NMR spectra of C:E:M1:P2_{80%} before catalysis and (b) ¹³C CP-MAS SELTICS NMR spectra of C:E:M1:P2_{80%} after continuous flow catalysis.

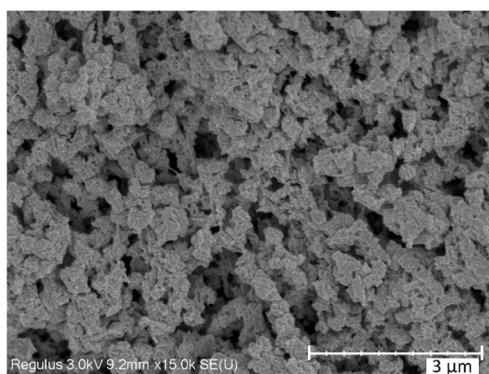


Figure S.25. Textural appearance of the interior of beads C:E:M1:P2_{80%} (after continuous flow catalysis), by SEM imaging (scale bar: 3 μm).

Table S. 9. Textural properties evaluated by nitrogen adsorption-desorption of the *AEROPIL* C:E:M1:P2_{80%} after catalysis. Notation: *a*_{BET}, specific surface area by the BET method; *V*_{P,BJH}, overall specific pore volume obtained by the BJH method; *V*_{mes}, specific mesopore volume; *D*_{P,BJH}, mean pore diameter by the BJH method.

Entry	Particles	<i>a</i> _{BET} (m ² /g)	<i>V</i> _{P,BJH} (cm ³ /g)	<i>D</i> _{P,BJH} (nm)
1	C:E:M1:P2 _{80%} (after batch catalysis)	30 (2)	0.19 (0.01)	24.8 (1.2)
2	C:E:M1:P2 _{80%} (after continuous flow catalysis)	118 (6)	0.66 (0.03)	22.2 (1.1)

8.5 Catalytic cycle

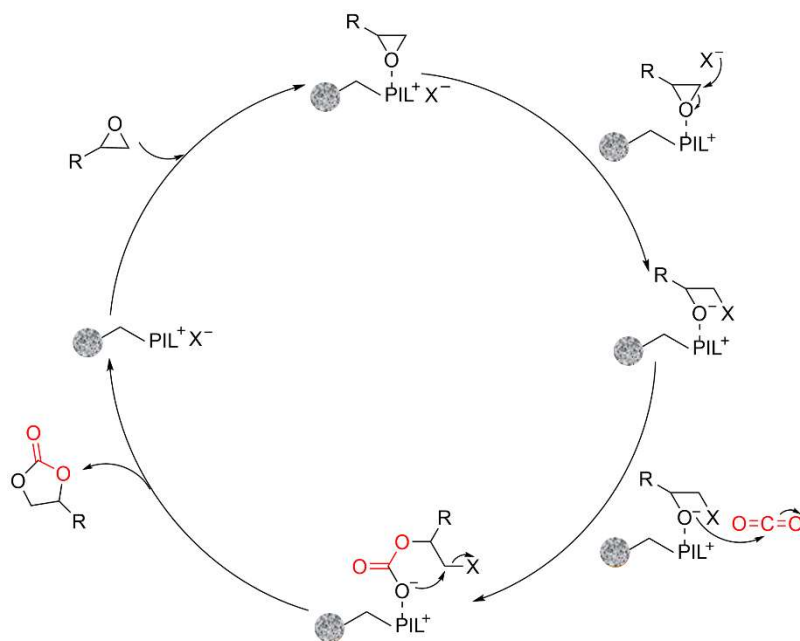


Figure S.26. Proposed catalytic mechanism for the CO₂ fixation with epoxides promoted by hydrogen-bond donors and Cl⁻ or Br⁻ anions in the *AEROPIL* catalyst (the interaction between the *AEROPIL* and the substrate is represented with dashed lines).

9 References

- [1] J. Tang, H. Tang, W. Sun, M. Radosz, Y. Shen, Low-pressure CO₂ sorption in ammonium-based poly(ionic liquid)s, *Polymer (Guildf)*. 46 (2005) 12460–12467. <https://doi.org/10.1016/j.polymer.2005.10.082>.
- [2] A. Zajac, A. Szpecht, D. Zielinski, K. Rola, J. Hoppe, K. Komorowska, M. Smiglak, Synthesis and characterization of potentially polymerizable amine-derived ionic liquids bearing 4-vinylbenzyl group, *J. Mol. Liq.* 283 (2019) 427–439. <https://doi.org/10.1016/j.molliq.2019.03.061>.
- [3] G. Yang, J. Yu, S. Peng, K. Sheng, H. Zhang, Poly(ionic liquid)-modified metal organic framework for carbon dioxide adsorption, *Polymers (Basel)*. 12 (2020).

- <https://doi.org/10.3390/polym12020370>.
- [4] X. Wang, J. Li, G. Chen, Z. Guo, Y. Zhou, J. Wang, Hydrophobic mesoporous poly(ionic liquid)s towards highly efficient and contamination-resistant solid-base catalysts, *ChemCatChem*. 7 (2015) 993–1003. <https://doi.org/10.1002/cctc.201402995>.
- [5] T.J. Cuthbert, T.D. Harrison, P.J. Ragona, E.R. Gillies, Synthesis, properties, and antibacterial activity of polyphosphonium semi-interpenetrating networks, *J. Mater. Chem. B*. 4 (2016) 4872–4883. <https://doi.org/10.1039/C6TB00641H>.
- [6] N.K. Mogha, N. Yadav, A. Sindhu, P. Venkatesu, Does poly(ionic liquid) modulate the non-covalent interactions of chicken egg white lysozyme? Elucidation of biomolecular interactions between biomolecules and macromolecular solvents, *New J. Chem.* 43 (2019) 16759–16766. <https://doi.org/10.1039/c9nj04078a>.
- [7] K.S.W. Sing, Reporting physisorption data for gas/solid systems with special reference to the determination of surface area and porosity (Recommendations 1984), *Pure Appl. Chem.* 57 (1985) 603–619. <https://doi.org/10.1351/pac198557040603>.
- [8] R. V. Barrulas, M. Zanatta, T. Casimiro, M.C. Corvo, Advanced porous materials from poly(ionic liquid)s: Challenges, applications and opportunities, *Chem. Eng. J.* 411 (2021) 128528. <https://doi.org/10.1016/J.CEJ.2021.128528>.
- [9] R. V. Barrulas, C. López-Iglesias, M. Zanatta, T. Casimiro, G. Mármol, M.R. Carrott, C.A. García-González, M.C. Corvo, The AEROPILs Generation: Novel Poly(Ionic Liquid)-Based Aerogels for CO₂ Capture, *Int. J. Mol. Sci.* 23 (2022) 200. <https://doi.org/10.3390/ijms23010200>.
- [10] A. Ayrál, J. Phalippou, T. Woignier, Skeletal density of silica aerogels determined by helium pycnometry, *J. Mater. Sci.* 27 (1992) 1166–1170. <https://doi.org/10.1007/BF01142014>.
- [11] G. Sneddon, A.Y. Ganin, H.H.P. Yiu, Sustainable CO₂ Adsorbents Prepared by Coating Chitosan onto Mesoporous Silicas for Large-Scale Carbon Capture Technology, *Energy Technol.* 3 (2015) 249–258. <https://doi.org/10.1002/ente.201402211>.
- [12] A.F. Eftaiha, A.K. Qaroush, A.K. Hasan, K.I. Assaf, F.M. Al-Qaisi, M.E. Melhem, B.A. Al-Maythalony, M. Usman, Cross-linked, porous imidazolium-based poly(ionic liquid)s for CO₂ capture and utilisation, *New J. Chem.* 45 (2021)

- 16452–16460. <https://doi.org/10.1039/D1NJ02946K>.
- [13] Y. Gao, L. Gu, Y. Qin, X. Wang, F. Wang, Dicarboxylic acid promoted immortal copolymerization for controllable synthesis of low-molecular weight oligo(carbonate-ether) diols with tunable carbonate unit content, *J. Polym. Sci. Part A Polym. Chem.* 50 (2012) 5177–5184. <https://doi.org/10.1002/pola.26366>.
- [14] A. Duval, L. Avérous, Cyclic Carbonates as Safe and Versatile Etherifying Reagents for the Functionalization of Lignins and Tannins, *ACS Sustain. Chem. Eng.* 5 (2017) 7334–7343. <https://doi.org/10.1021/acssuschemeng.7b01502>.
- [15] W. Luo, J. Qin, M. Xiao, D. Han, S. Wang, Y. Meng, Synthesis of Aliphatic Carbonate Macrodiols and Their Application as Sustainable Feedstock for Polyurethane, *ACS Omega.* 2 (2017) 3205–3213. <https://doi.org/10.1021/acsomega.7b00183>.
- [16] L.G. Ding, B.J. Yao, F. Li, S.C. Shi, N. Huang, H.B. Yin, Q. Guan, Y. Bin Dong, Ionic liquid-decorated COF and its covalent composite aerogel for selective CO₂ adsorption and catalytic conversion, *J. Mater. Chem. A.* 7 (2019) 4689–4698. <https://doi.org/10.1039/c8ta12046c>.
- [17] M. Taheri, M. Ghiaci, A. Shchukarev, Cross-linked chitosan with a dicationic ionic liquid as a recyclable biopolymer-supported catalyst for cycloaddition of carbon dioxide with epoxides into cyclic carbonates, *New J. Chem.* 42 (2018) 587–597. <https://doi.org/10.1039/C7NJ03665E>.
- [18] H. Zhong, J. Gao, R. Sa, S. Yang, Z. Wu, R. Wang, Carbon Dioxide Conversion Upgraded by Host-guest Cooperation between Nitrogen-Rich Covalent Organic Framework and Imidazolium-Based Ionic Polymer, *ChemSusChem.* (2020) cssc.202001658. <https://doi.org/10.1002/cssc.202001658>.
- [19] C. Bao, Y. Jiang, L. Zhao, D. Li, P. Xu, J. Sun, Aminoethylimidazole ionic liquid-grafted MIL-101-NH₂ heterogeneous catalyst for the conversion of CO₂ and epoxide without solvent and cocatalyst, *New J. Chem.* 45 (2021) 13893–13901. <https://doi.org/10.1039/D1NJ02590B>.
- [20] Y.-R. Du, G.-R. Ding, Y.-F. Wang, B.-H. Xu, S.-J. Zhang, Construction of a PPIL@COF core-shell composite with enhanced catalytic activity for CO₂ conversion, *Green Chem.* 23 (2021) 2411–2419. <https://doi.org/10.1039/D1GC00267H>.
- [21] Y.-R. Du, X. Yang, Y.-F. Wang, P.-X. Guan, R. Wang, B.-H. Xu, Immobilization poly(ionic liquid)s into hierarchical porous covalent organic frameworks as

- heterogeneous catalyst for cycloaddition of CO₂ with epoxides, *Mol. Catal.* 520 (2022) 112164. <https://doi.org/10.1016/j.mcat.2022.112164>.
- [22] H. He, Q. Zhu, W. Zhang, H. Zhang, J. Chen, C. Li, M. Du, Metal and Co-Catalyst Free CO₂ Conversion with a Bifunctional Covalent Organic Framework (COF), *ChemCatChem*. 12 (2020) 5192–5199. <https://doi.org/10.1002/cctc.202000949>.
- [23] Y. Zhao, Y. Zhao, J. Qiu, Z. Li, H. Wang, J. Wang, Facile Grafting of Imidazolium Salt in Covalent Organic Frameworks with Enhanced Catalytic Activity for CO₂ Fixation and the Knoevenagel Reaction, *ACS Sustain. Chem. Eng.* 8 (2020) 18413–18419. <https://doi.org/10.1021/acssuschemeng.0c05294>.
- [24] J. Qiu, Y. Zhao, Z. Li, H. Wang, Y. Shi, J. Wang, Imidazolium-Salt-Functionalized Covalent Organic Frameworks for Highly Efficient Catalysis of CO₂ Conversion, *ChemSusChem*. 12 (2019) cssc.201900570. <https://doi.org/10.1002/cssc.201900570>.